



# **BRNO UNIVERSITY OF TECHNOLOGY**

VYSOKÉ UČENÍ TECHNICKÉ V BRNĚ

## **FACULTY OF MECHANICAL ENGINEERING**

FAKULTA STROJNÍHO INŽENÝRSTVÍ

## **INSTITUTE OF PHYSICAL ENGINEERING**

ÚSTAV FYZIKÁLNÍHO INŽENÝRSTVÍ

# **DIELECTRIC METASURFACES AS MODERN OPTICAL COMPONENTS**

DIELEKTRICKÉ METAPOVRCHY JAKO MODERNÍ OPTICKÉ PRVKY

## **MASTER'S THESIS**

DIPLOMOVÁ PRÁCE

### **AUTHOR**

AUTOR PRÁCE

**Bc. Katarína Rovenská**

### **SUPERVISOR**

VEDOUCÍ PRÁCE

**Ing. Filip Ligmajer, Ph.D.**

**BRNO 2020**



# Specification Master's Thesis

Department: Institute of Physical Engineering  
Student: **Bc. Katarína Rovenská**  
Study programme: Applied Sciences in Engineering  
Study branch: Physical Engineering and Nanotechnology  
Supervisor: **Ing. Filip Ligmajer, Ph.D.**  
Academic year: 2019/20

Pursuant to Act no. 111/1998 concerning universities and the BUT study and examination rules, you have been assigned the following topic by the institute director Master's Thesis:

## **Dielectric metasurfaces as modern optical components**

### **Concise characteristic of the task:**

Manipulation of light beams is most often done using conventional optical components like lenses or polarizers, which are bulky and suffer from imperfections. Metasurfaces are a modern alternative to these components, which offers subwavelength thickness or even unprecedented optical functions unseen in natural materials. While the first real examples of metasurfaces were composed of building blocks made of nanostructured metals, the promise of better efficiency led recently to exploration of metasurfaces formed by dielectric nanostructures. In line with this trend, the goal of this work will be fabrication and characterization of dielectric metasurfaces with practically relevant optical functions like phase plates or beam splitters.

### **Goals Master's Thesis:**

1. Based on the literature review and, optionally, on the numerical simulations select the suitable materials, shapes and dimensions of the building blocks for dielectric metasurfaces with functions like phase plate or beam splitter.
2. Fabrication and characterization of samples of the individual building blocks for the future dielectric metasurface.
3. Fabrication of the full dielectric metasurface and its characterization with respect to the target optical function.

### **Recommended bibliography:**

KHORASANINEJAD, Mohammadreza a Federico CAPASSO, 2017. Metalenses: Versatile multifunctional photonic components. Science. 358(6367). DOI: 10.1126/science.aam8100.

LALANNE, Philippe a Pierre CHAVEL, 2017. Metalenses at visible wavelengths: past, present, perspectives. 11(3). DOI: 10.1002/lpor.201600295.

Deadline for submission Master's Thesis is given by the Schedule of the Academic year 2019/20

In Brno,

L. S.

---

prof. RNDr. Tomáš Šikola, CSc.  
Director of the Institute

---

doc. Ing. Jaroslav Katolický, Ph.D.  
FME dean



## ABSTRACT

Thanks to their high versatility and low spatial demands, metasurfaces are promising as replacements of traditional optical components. Within this thesis, attention is brought mostly to the metasurfaces which can replace half wave plates and diffractive beam splitters. Two strategies for fabrication of high-aspect ratio nanostructures from titanium dioxide are demonstrated – one employing reactive ion etching of  $\text{TiO}_2$  layer through a metallic hardmask, the other using a patterned electron resist as a mold for atomic layer deposition of  $\text{TiO}_2$ . The optical properties of the fabricated structures, such as phase shift and transmissivity, are also characterized and analyzed.

## KEYWORDS

metasurfaces,  $\text{TiO}_2$ , nanostructure fabrication, phase measurements

## ABSTRAKT

Vďaka ich vysokej verzatilite a nízkej priestorovej náročnosti sú metapovrchy sľubným nasledovníkom tradičných optických komponentov. Táto práca sa upriamuje na metapovrchy, ktoré môžu nahradiť polvlnné doštičky a difraktívne deliče zväzku. Práca prezentuje dve stratégie výroby nanoštruktúr z oxidu titaničitého s vysokým pomerom strán – jedna používa reaktívne iónové leptanie vrstvy  $\text{TiO}_2$  skrz kovovú masku, kým druhá používa štrukturovaný elektrónový rezist ako formu pre depozíciu atomárnych vrstiev  $\text{TiO}_2$ . V závere práce sú charakterizované a analyzované optické vlastnosti vyrobených štruktúr, predovšetkým ich fázový posun a transmisivita.

## KLÍČOVÁ SLOVA

metapovrchy,  $\text{TiO}_2$ , výroba nanoštruktúr, fázové merania

ROVENSKÁ, Katarína. *Dielectric metasurfaces as modern optical components*. Brno, 2020. 57 p. Diploma thesis. Brno University of Technology. Faculty of Mechanical Engineering. Supervised by Filip Ligmajer.



Prehlasujem, že som túto diplomovú prácu vypracovala samostatne pod odborným vedením Ing. Filipa Ligmajera, PhD., a že všetky podklady, z ktorých som čerpala, sú uvedené v zozname použitej literatúry.

Bc. Katarína Rovenská



Predovšetkým ďakujem Ing. Filipovi Ligmajerovi, PhD., za príkladné vedenie mojej práce, za jeho ochotu, pomoc a čas, ktoré mi venoval nielen pri konzultovaní a pripomienkovaní tejto práce, ale tiež pri rezaní substrátov. Filip, Tvoj prístup si veľmi cením a ďakujem.

Členovia našej plazmonickej skupiny, no hlavne Ing. Martin Hrtoň, Ing. Petr Dvořák, PhD., a Mgr. Jiří Liška, PhD.: som vdáčná, že som s Vami mohla konzultovať teoretické i praktické aspekty výroby metapovrchov. Za pomoc s CCHM meraniami a diskusiu o ich výsledkoch by som rada poďakovala Ing. Miroslavovi Ďurišovi a Ing. Petrovi Bouchalovi, PhD.. Ústavu prístrojovej techniky Akadémie vied Českej republiky ďakujem za spoluprácu a výrobu rezistovej masky pre ALD. Prof. RNDr. Jiřímu Spoustovi, PhD., ďakujem za cenné pripomienky k textu tejto práce.

Spolupracovníci a priatelia z laboratórií CEITEC Nano RI a Ústavu fyzikálního inženýrství FSI VUT, najmä Ondra, Kuba, Tesi, Ivoš, Tom, Andrej, Lucka, Igor, Mára, Veronika, ale tiež všetci ostatní: ďakujem za rady i milé slová. Aj vďaka vám robím svoju prácu ešte o niečo radšej.

Mojej rodine ďakujem za poskytnuté zázemie, podporu, záujem a trpezlivosť, nielen počas písania tejto práce, ale i počas celého môjho štúdia.

Táto práca bola realizovaná za podpory výskumnej infraštruktúry CzechNanoLab (ID LM2018110, MŠMT, 2020–2022), CEITEC Vysoké učení technické v Brně.



# CONTENTS

<b>1</b>	<b>Introduction</b>	<b>3</b>
<b>2</b>	<b>Theory of metasurfaces</b>	<b>5</b>
2.1	What are metasurfaces . . . . .	5
2.1.1	Metasurfaces - applications in optics . . . . .	7
2.2	Basics of designing optical metasurfaces . . . . .	9
2.3	Metasurfaces as optical devices counterparts . . . . .	11
2.3.1	Half-wave plate . . . . .	11
2.3.2	Diffractive beam splitter . . . . .	12
2.4	Characterization of metasurfaces . . . . .	13
2.4.1	Coherence-controlled holographic microscopy . . . . .	13
2.4.2	Optical spectroscopy . . . . .	16
<b>3</b>	<b>Methods for sample fabrication</b>	<b>19</b>
3.1	Thin film deposition of oxides and metals . . . . .	19
3.1.1	Atomic layer deposition . . . . .	19
3.1.2	Magnetron sputtering . . . . .	21
3.1.3	Evaporation . . . . .	23
3.2	Electron beam lithography . . . . .	25
3.2.1	Spin-coating . . . . .	26
3.2.2	Patterning with an electron beam . . . . .	28
3.2.3	Resist development . . . . .	29
3.3	Etching . . . . .	29
3.3.1	Wet etching . . . . .	30
3.3.2	Reactive ion etching . . . . .	31
<b>4</b>	<b>Results</b>	<b>33</b>
4.1	Sample fabrication . . . . .	34
4.1.1	Other fabrication results . . . . .	42
4.2	Optical characterization of the metasurfaces . . . . .	44
<b>5</b>	<b>Conclusions</b>	<b>51</b>
	<b>References</b>	<b>53</b>





# 1 INTRODUCTION

An interest in the topic of light propagation originates in ancient India. Later, about 300 BC, Euclides introduced his interpretation of geometrical optics and Hero presented his theory on the universal principle of paths taken by light in order to propagate: the Hero's principle of shortest path. In 1679, Fermat refined this approach and introduced the Fermat's principle of least time. In 2011, Capasso's group at Harvard revisited the Snell's laws of reflection and refraction given by the Fermat's principle. In the generalized laws of reflection and refraction presented by this group [1], abrupt phase variations of light are introduced, which can alter the path of propagating light in a way uncommon for the traditional optics. Additionally, these phase jumps, as they are often denoted, enable precise control of light wavefronts by tailoring the amplitude and phase of light. One of the most common ways to incorporate such abrupt phase variations into light is via metasurfaces. Usually, metasurfaces are created by careful placing of many small subwavelength structures on a substrate. Through the design of these metasurface building blocks, various functionalities of metasurfaces can be achieved, and metasurfaces may serve as planar alternatives for traditional optical components, which is, eventually, the topic of this work.

Within this thesis, attention is brought mostly to the fabrication and optical characterization of metasurface counterparts of a half-wave plate and a diffractive beam splitter. These components were selected upon their practical abilities of light polarization control and wavefront control suitable for generating large arrays of identical light beams, respectively. The presented thesis is structured into the following chapters:

In chapter 2, the theoretical background and applications of metasurfaces are described. Further, attention is brought to the process of designing a metasurface – the methods used for phase tuning in metasurfaces are discussed along with properties of metasurface building blocks, which affect the optical response of the metasurface. Finally, methods for optical characterization of metasurfaces are introduced, which were used to analyze the performance of the metasurfaces fabricated within this work.

Chapter 3 presents a selection of techniques and instrumentation for the fabrication of metasurfaces. First, thin film deposition methods are addressed. Then, electron beam lithography is introduced, along with spin-coating, resist development, and chemistry related to these topics. At the end of this chapter, reactive ion etching and wet etching are discussed.

Chapter 4 summarizes the experimental part of this work. The fabrication process is presented in a great detail, along with experiments performed in order to

prove the quality of the individual fabrication steps. The results of the optical measurements of the fabricated structures are demonstrated, too.

Finally, chapter 5 provides the conclusion of this thesis. The most significant outcomes of the experimental work on fabrication and optical characterization of the presented structures are reminded to the reader along with their contribution to further metasurface fabrication at Brno University of Technology. At last, the possible advancements of this work are discussed.

## 2 THEORY OF METASURFACES

Originating in Greek, a prefix *meta*- commonly either denotes changes (metabolism, metaphor, metamorphose,...) or a state of being above and beyond (metaphysics, metahuman in pop-culture,...). In metasurfaces, the prefix takes the latter meaning, pointing to a fact that surfaces can be innovated towards non-elementary purposes, such as field enhancement or wavefront control. This chapter will deal with a definition of metasurfaces, a description of their capabilities and applications alongside with some of their main working principles. Further, attention will be brought to specific optical devices and their metasurface counterparts, which were eventually fabricated and characterized within this work.

### 2.1 What are metasurfaces

A majority of literature opens the discussion about metasurfaces by stating their relation to metamaterials, claiming that metasurfaces are a two-dimensional alternation of metamaterials. [2–5] Indeed, the description of a metamaterial as of an artificially structured material that exhibits extraordinary electromagnetic properties not available or not easily obtainable in nature [6] can be used to describe metasurfaces, too. For some, metasurfaces are understood as an evolutionary stage of metamaterials, which were developed to facilitate the fabrication of three-dimensional objects filled with subwavelength-sized structures, i.e., metamaterials. In summary, metasurfaces offer low-lossy, easier to fabricate, and more integrable alternative of metamaterials.

The advantageous character of metasurfaces has assured for an impressive range of applications, such as electric field enhancement [7, 8], wavefront shaping [9], tailoring of the phase, amplitude, polarization of light [10, 11], etc. However, all of the mentioned functionalities can be delivered to us by objects and devices known for decades, even longer in the case of sole optical devices. Thus, a question arises, what is the novelty of a metasurface in comparison to the known instrumentalities?

To control the optical path of light, conventional optical devices rely on propagation of light through media of a given refractive index and a given thickness. Lenses accumulate the phase changes of the light, while it propagates through distances much larger than the operational wavelength. Waveplates pile up the polarization changes along the propagation of light through the device to achieve any desired polarization.

Metasurfaces, on the other hand, introduce abrupt changes of optical properties of light [1, 3, 12]. Electromagnetic waves passing through a metasurface undergo phase jumps on distances small compared to the wavelength of operation. The

phenomenon of a phase discontinuity originates in the minute, subwavelength size of individual building blocks forming a metasurface. [5]

In general, the propagation of light is governed by the Fermat's principle of least time. In his lectures [13], Feynman expresses this principle in a drowning man's dilemma: Should a lifeguard standing at the coast rescue a man drowning in the water, what would be the optimal route for the lifeguard to save the drowning man as quickly as possible? Capasso group enriched this analogy with a stone wall of varying height, which impersonates the phase jump embodied by the metasurface. [3] Fig. 1a shows how the optimal trajectory of the lifeguard (light beam) changes with the presence of a stone wall (phase jump) at the interface of the two media, in accordance to the presented dilemma. In optics, such optimal trajectory was described in [1] by generalized laws of refraction:

$$n_t \sin \vartheta_t - n_i \sin \vartheta_i = \frac{\lambda_0}{2\pi} \frac{d\Phi}{dx}, \quad \cos \vartheta_t \sin \varphi_t = \frac{\lambda_0}{2\pi n_t} \frac{d\Phi}{dy}, \quad (1)$$

and reflection:

$$\sin \vartheta_r - \sin \vartheta_i = \frac{\lambda_0}{2\pi n_i} \frac{d\Phi}{dx}, \quad \cos \vartheta_r \sin \varphi_r = \frac{\lambda_0}{2\pi n_i} \frac{d\Phi}{dy}, \quad (2)$$

where:  $n_t$  and  $n_i$  are, respectively, the indices of refraction at the incident and the transmission side of the metasurface, all angles are defined in Fig. 1b,  $\lambda_0$  is the operational wavelength in vacuum, and  $d\Phi/dx$ ,  $d\Phi/dy$  are the components of the phase gradient parallel and normal to the plane of the incidence, respectively. Indeed,

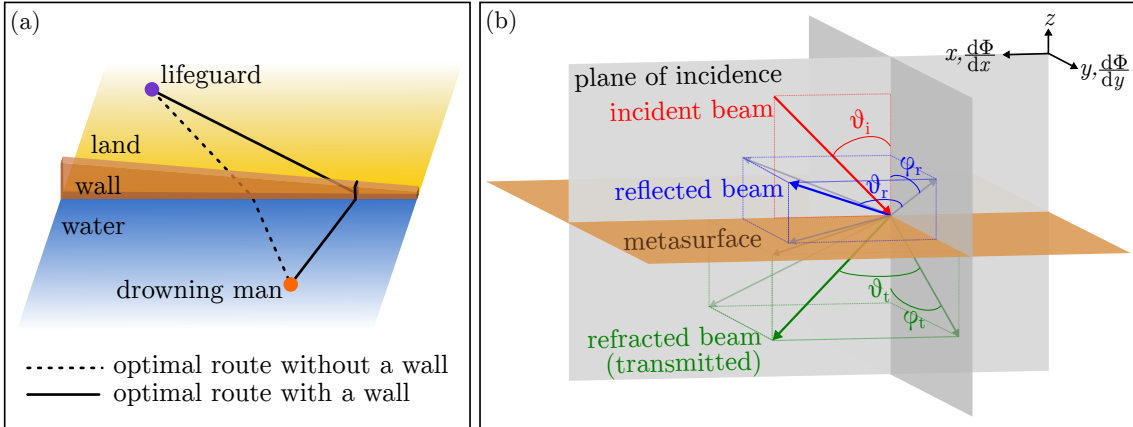


**Figure 1:** (a) The drowning man dilemma enriched by a wall of varying height at the interface of two media, resembling of phase discontinuity of a metasurface. The optimal trajectory changes in accordance with Fermat's principle of least time as the wall is added to the scheme. (b) Definition of geometry for generalized laws of refraction and reflection. Reflected (blue, index "r") and refracted (green, index "t") beams can be engineered into any arbitrary direction by phase gradient  $d\Phi/dx$ . Inspired by [1, 3]

should the phase remain constant across the media interface, equations (1), (2) would regain the form of Snell’s laws of refraction and reflection, respectively. Still, generalized laws of refraction and reflection point out that the incident beam of light can be moulded by a metasurface into any desired response, reflected or transmitted. This enables a variety of functionalities and applications for the metasurfaces, some of which are shortly reviewed in the following text.

### 2.1.1 Metasurfaces - applications in optics

Conventional optical devices can often be spatially demanding, which makes the use of metasurfaces, compact and flat devices, very advantageous. Furthermore, there is high versatility of metasurfaces caused by freedom in the designing of the building blocks which form it. Thus, almost any optical component can have a metasurface counterpart. Nowadays, the image quality and efficiency of such metasurface counterparts do not always meet the standards set by traditional optics. However, the field of ”flat optics”, as are metasurface-based optical components often denoted, grows rapidly, and the enhancement of said traits is expected [12,14]. To introduce some of the tremendous number of metasurfaces developed in recent years, Fig. 2 shows a few selected metasurfaces with various functionalities.

In Fig. 2a, two main approaches for phase control using metasurfaces are combined: the propagation phase and geometric phase – for further discussion on phase control in metasurfaces, see section 2.2. By each of these phase modification systems, different phase profiles can be imprinted into the metasurface. In the case of the propagation phase method, an arbitrary phase profile can be engineered on each of the two orthogonal linear polarizations of the incident light. With the geometric phase technique, only the original phase profile and its counterpart (not two arbitrary phase profiles) can be carried by the two opposite circular polarizations. In [15], a combination of these two approaches is used to create a hologram supporting an elliptical polarization. Two phase profiles are embedded into the design of the metasurface, distinguishable when illuminated by chirally opposite sources. This would be impossible with conventional optics, and supports the superiority of metasurfaces over conventional optics for the future development.

Fig. 2b shows the design of a metasurface lens capable of correcting chromatic aberrations in the optical range. [16] The layers forming this metasurface differ in used materials, sizes, and periodicity of the building blocks. This ensures that by each layer, only lightbeams of a specific wavelength are affected and are led into a focal point 1 mm away from the device. Since late 2018, there are also single-layered metasurfaces which can focus a broad band of wavelengths. [17]

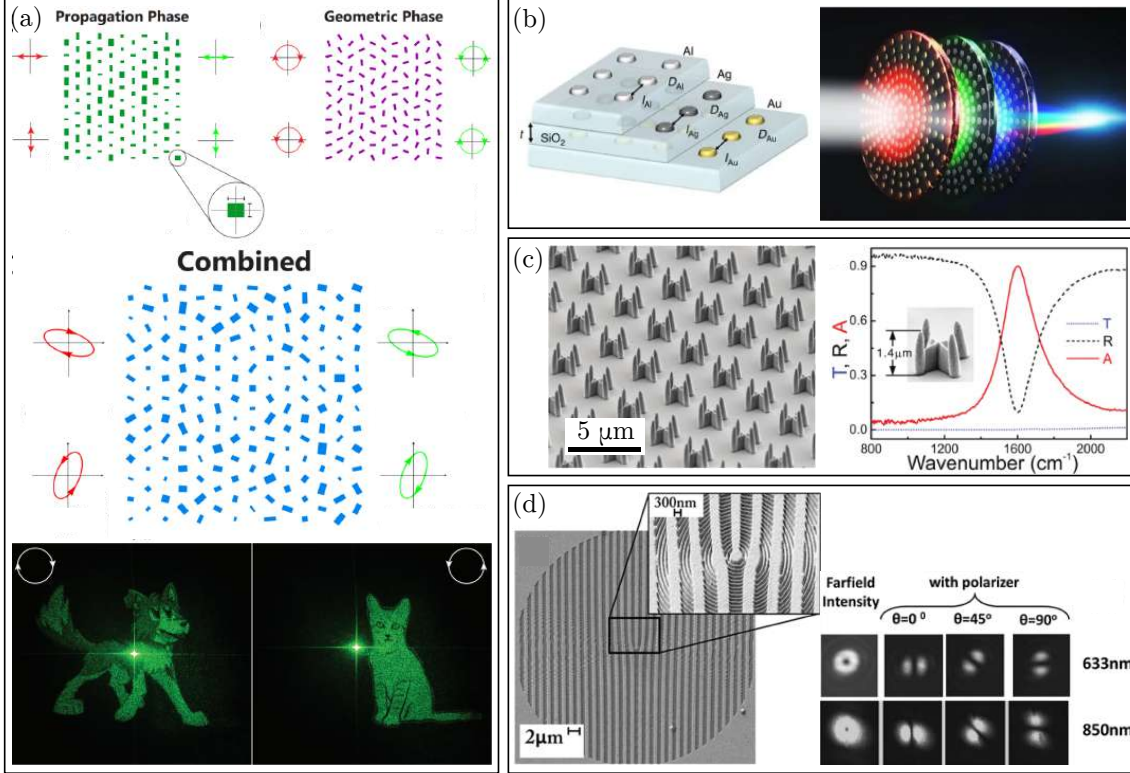


**Figure 2:** (a) Combination of propagation phase and geometric phase enables to incorporate two independent phase profiles into a hologram created by the metasurface. Adapted from [15]. (b) Three-layered metasurface serving for correction of the chromatic aberrations. Adapted from [16]. (c) Metasurface engineered to achieve close-to-unity absorption. Adapted from [18]. (d) Simultaneous steering of the amplitude, phase and polarization of light in broad frequency range. Adapted from [19].

A further application of metasurfaces can be found in engineering of the reflection, transmission, or absorption of electromagnetic radiation. Fig. 2c introduces a perfectly absorbing metasurface working in the mid-infrared region. Apart from other metasurfaces, which use a metal-dielectric multilayer to achieve phase shift supported by resonant structures, ref. [18] presents building blocks that support the resonance in the space between the arms of the resonant structure. This way, the spectral position of the absorbance peak can be tuned by varying the height of the structure arms, and absorbance up to 90% can be achieved. [18]

Lastly, Fig. 2d depicts a metasurface capable of simultaneous tuning of phase, amplitude, and polarization of the incident light. The novelty of this metasurface lies in replacing the large openings of conventional holograms by arrays of subwavelength apertures, oriented to locally select a particular state of polarization. Such control can be achieved for a broad wavelength range with a single metasurface design. [19]

## 2.2 Basics of designing optical metasurfaces

The impressive range of applications supported by metasurfaces stems mostly from the versatility of their building blocks. By careful designing of the constitutional units which spatially vary phase shifts embodied by metasurfaces, devices with unique functionalities can be engineered. In the following, principles which support the phase tailoring will be introduced. Further, attributes of metasurface building blocks will be presented along with notes on how they affect the optical response of a metasurface.

To alter the functionality of an optical metasurface, mostly the spatial variations of the phase shift caused by the metasurface building blocks phase are used, as referenced in section 2.1. To achieve such tailoring of the phase, two main approaches have been reported: the implementation of resonant nanoantennas [20–22] or introduction of the propagation phase delay [23, 24]. However, these methods might not suffice for each metasurface to provide the phase modulation across a full  $2\pi$  interval. Hence, they are often combined with the Pancharatnam-Berry (geometric) phase technique which increases the phase modulation interval of each of the two methods, see [1, 14, 25]. For a brief overview of these phase altering techniques, see Fig. 3.

Metasurfaces which modify their phase shift with the use of resonant nanoantennas can be further distinguished upon the type of the supported resonance: plasmonic resonators or dielectric resonators which carry Mie resonances. Commonly, metasurfaces composed of metallic resonators achieve low efficiency at visible wave-

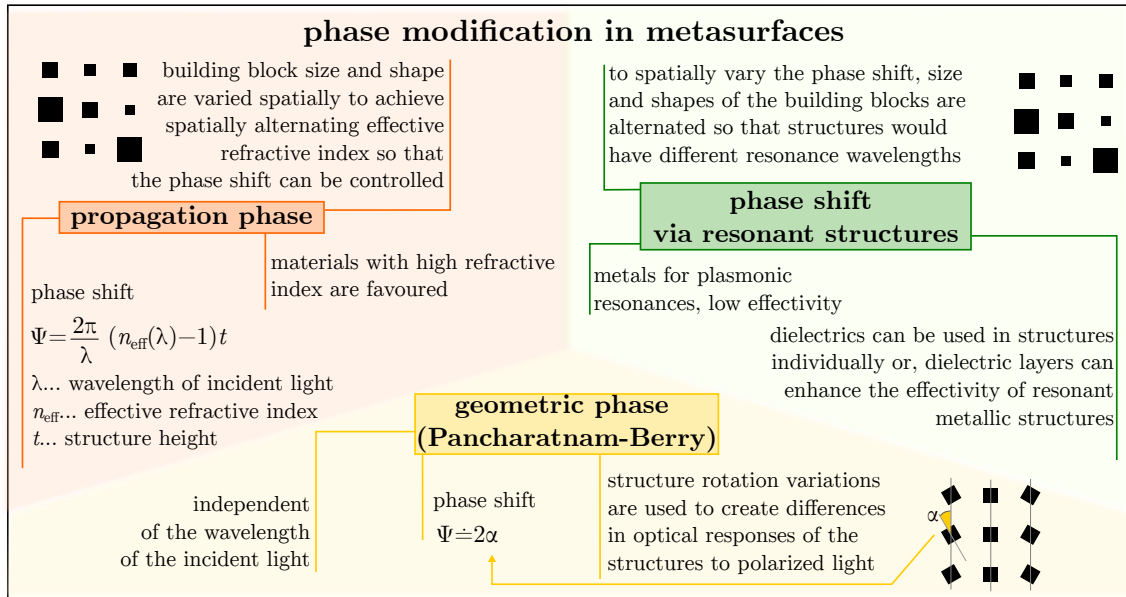


**Figure 3:** Overview of phase modification techniques used in metasurfaces.



lengths. However, the improvement of their efficiency was reported with the use of multilayer, dielectric-containing systems. [26, 27] In general, metasurfaces based on dielectric resonators tend to be more effective than those based on plasmonic resonators across the UV-NIR wavelengths. [28] Regarding the design of such metasurfaces, the size of the individual building blocks is varied so that the resonances of these structures occur at different wavelengths. Hence, for a specific wavelength of the incident light, the phase profile embodied by the metasurface can be engineered as desired.

Another approach to phase modification is the implementation of the propagation phase. Even in a simple system of a layer on the substrate, some phase shift  $\Psi$  would be caused by the mere presence of this layer on the substrate instead of air (vacuum). In case that the surrounding medium is air ( $n_{\text{air}} \doteq 1$ ), the phase delay  $\Psi$  caused by the propagation through a layer is:

$$\Psi = \frac{2\pi}{\lambda}(n(\lambda) - 1)t, \quad (3)$$

where  $\lambda$  is the wavelength of the used irradiation,  $n(\lambda)$  is the refractive index of the material which forms the layer and  $t$  is the thickness of this layer. Propagation phase-based metasurfaces act similarly – however, to be able to control the refractive index of the layer spatially, the metasurface is composed of building blocks with varying subwavelength sizes. This way, the incident light encounters a spatially varying mixture of the refractive indices of the substrate, structures and, the surrounding medium, i.e., the effective refractive index of the metasurface,  $n_{\text{eff}}(\lambda)$ . Further, the final phase profile of this type of metasurfaces is dependent on the height of the building blocks, which must be selected carefully with respect to the wavelength of the incident light, the building block material, and the desired interval for phase modification. For propagation phase metasurfaces, dielectrics with high refractive index are favored as the building block material because they enable to fabricate the structures of relatively low height to achieve the desired phase shift.

The third common way to control the phase profile embodied by a metasurface is introduced by the geometric phase technique. To achieve variations in the optical responses of the structures so that the phase shift could be altered spatially, individual building blocks are rotated in the plane parallel to the substrate. Then, the metasurface responds differently to each polarization of the incident light. A significant advantage of the geometric phase is its independence on the wavelength of the incident light. Due to this property, the geometric phase can be easily combined with the propagation phase or with the phase shift of resonant structures.



## 2.3 Metasurfaces as optical devices counterparts

As discussed before, conventional optical devices could be replaced with optical metasurfaces in the future. The metasurface variants of conventional optical devices are less spatially demanding and further, brand new functionalities can be achieved in comparison to the conventional optics. [15] Nowadays, the possible applications of optical metasurfaces are still being explored. In the following text, two applications of the optical metasurfaces will be introduced: half-wave plate and diffractive beam splitter. These optical components have been chosen as they were fabricated and characterized within this work (see chapter 4).

### 2.3.1 Half-wave plate

Waveplates are used mostly for polarization control in optical setups. Conventionally, polarization of the incident light is changed due to the accumulated phase difference achieved by propagation of light through a thick layer of birefringent material. As metasurfaces introduce abrupt phase jumps, the bulky components can be substituted with a metasurface designed to alter the phase of incident light so that its polarization would be changed by a given value.

In the case of half-wave plate, the difference between the polarization of the incident and the transmitted beam should be  $\pi/2$ , as illustrated in Fig. 4a. For a metasurface counterpart of this optical device, the spatial variation of the phase shift is not needed, the entire functional area should have a single value of the embodied phase. To provide the necessary polarization conversion, anisotropic structuring of the sample surface is used. In the past years, the majority of the proposed half-wave plates have operated in near-IR to THz spectral region. The experimentally realized building blocks were high aspect ratio silicon pillars with rectangular profiles [29], rectangular Au- nanopatches enclosed by Si substrate and Si superstrate [30], or gold rectangular resonators separated from a gold film by silicon dioxide layer [31]. Despite the troublesome fabrication of nano-sized metasurface building blocks usable at optical frequencies, metasurface half-wave plates operating in the visible spectrum were presented in the literature already. Some of the proposed metasurfaces included circular grooves in a silver film with a triangular profile on silicon substrate [32] and gold L-shaped resonators on a gold ground layer [33].

For the purposes of this thesis, half-wave plate metasurfaces for optical frequencies were designed as an array of high-aspect ratio wall-like  $\text{TiO}_2$  building blocks (for further discussion, see chapter 4).

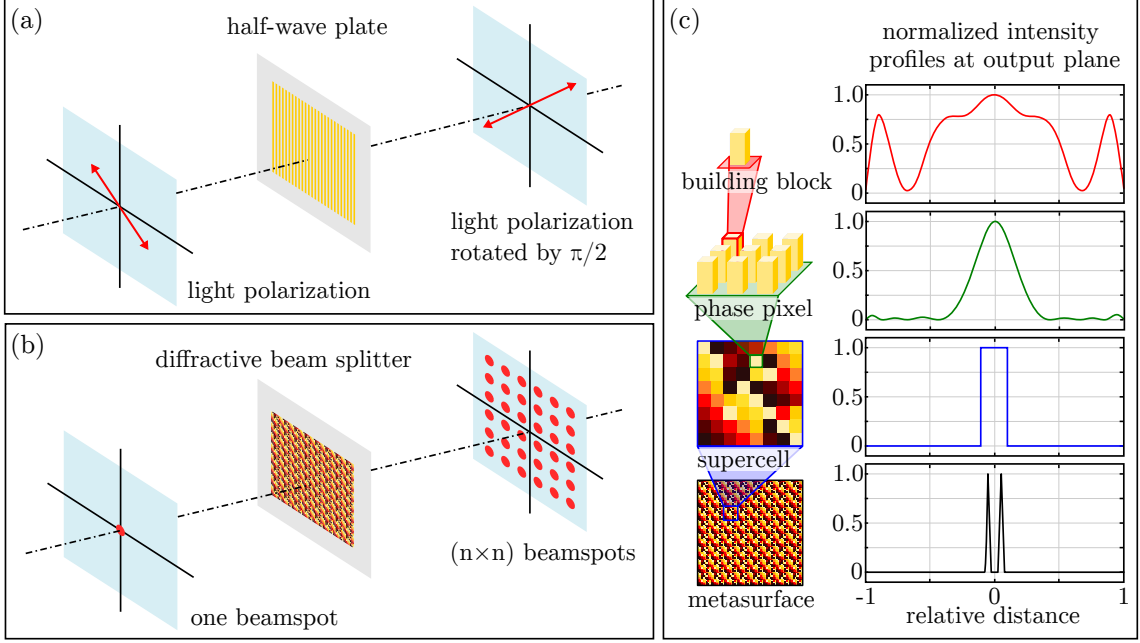


**Figure 4:** Metasurface counterparts of selected optical components. (a) A schematic of a metasurface-based half-wave plate and its functionality. (b) A schematic of a metasurface-based diffractive beam splitter and its functionality. (c) Main principle of designing a diffractive beam splitter. The metasurface is composed of smaller building units – supercells, phase pixels, building blocks. M. Hrtoň is gratefully acknowledged for his involvement in the development of this panel.

### 2.3.2 Diffractive beam splitter

A diffractive beam splitter serves for the defined division of a single beam into several mutually diverging beams, as shown in Fig. 4b. Traditional methods of generating such beam arrays involve diffractive optical elements and spatial light modulators. [34] In the alternative (metasurface) approach, a phase profile can be imprinted into the metasurface, so that in the output plane, only the desired diffraction maxima would appear. Recently, such metasurfaces were developed for visible light from silicon/silica [35] and titanium oxide/silica [36].

To design such a device, the metasurface building blocks (see Fig. 4c, marked by red) are first arranged into phase pixels (green in Fig. 4c). A phase pixel is a set of several identical metasurface building blocks. The presence of multiple blocks of the same kind assures the narrowing of the beamspot in the output plane, as shown in Fig. 4c. Further, various phase pixels can be arrayed into a “supercell” (blue in Fig. 4c), which further supports narrowing of the light intensity profile at the output plane. Finally, the intensity profiles can be limited to several desired delta functions by arranging multiple supercells in the functional area of the metasurface (black in Fig. 4c).

For a successful design of such metasurface, the phase shift caused by individual phase pixels must be known. The behavior of individual building blocks can be simulated numerically. However, especially with nano-sized building blocks, attention must be paid to the fabrication imperfections in structure fabrication, which can hardly be implemented into the simulations without experimental background. Hence, two types of building blocks (with lateral profile of a circle or a square) with varying sizes have been fabricated in this work and the phase shift caused by them was determined experimentally (see chapter 4).

## 2.4 Characterization of metasurfaces

To analyze the performance of optical metasurfaces, various methods can be used, depending on the functionality of the metasurface or the principle which provides the metasurface with its embodied phase shift. In the following, coherence-controlled holographic microscopy will be introduced as one of the means to quantify the phase shift of a metasurface. As this method proved to be inaccurate for establishing of the variations in the amplitude of the metasurface-altered light in this thesis (see section 4.2 for more detailed explanation), far-field spectroscopy will be described as a method for characterization of the metasurface transmissivity.

### 2.4.1 Coherence-controlled holographic microscopy

In all light-based microscopes, formation of an image depends on the interference of direct and diffracted light in the image plane. However, common microscopes are not able to determine the phase difference introduced by the studied sample. Nowadays, such quantitative phase measurements are feasible with interference microscopy techniques such as phase stepping interferometry (PSI) or digital holographic microscopy (DHM). In these techniques, the interference of (usually) two light beams – the reference beam and the beam interacting with the studied object – at the output plane enables to quantify the phase shift introduced by the studied sample. [37] In PSI, the reference beam and object beam are parallel and thus, light sources of low-coherence can be used. To reconstruct the amplitude and phase of the object wave in PSI, a set of measurements with varying phase shift must be performed. On the other hand, DHM often introduces a small angle between reference and object beams. The complex amplitude of the reference beam in the output plane is thus enriched by a spatially varying phase shift – hence, only a single measurement suffices for the reconstruction of the sample hologram. Coherence-controlled holographic microscope (CCHM), designed at BUT, combines the both approaches in such a way that a single measurement is enough for the hologram reconstruction and high spatial and

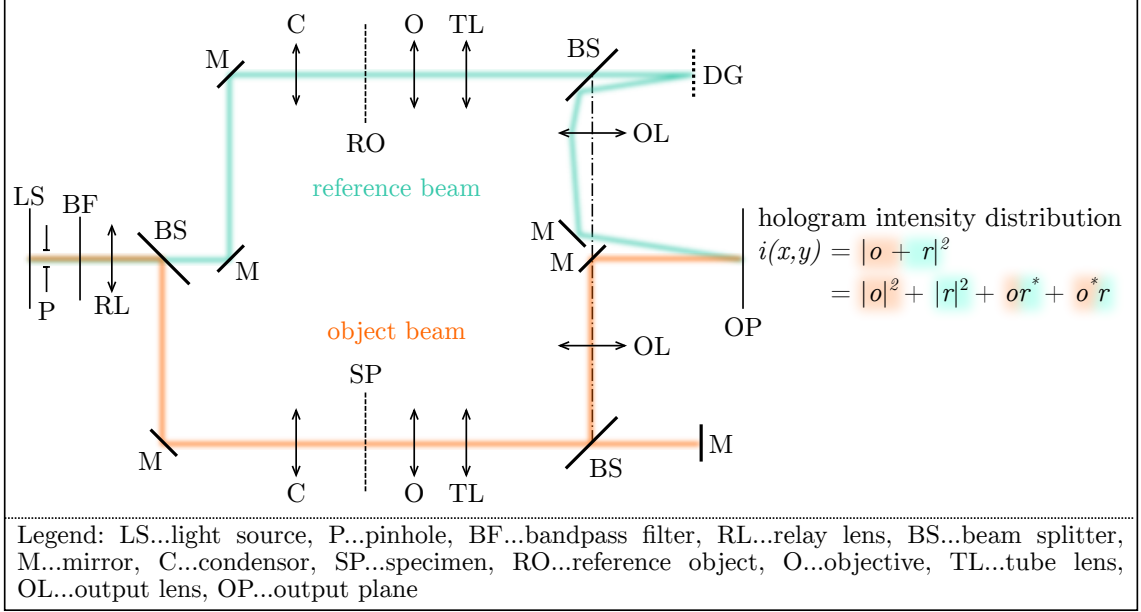


**Figure 5:** Schematic of the coherence-controlled holographic microscope designed at BUT. Adapted from [38].

temporal coherence are not required from the used light sources. [38] In fact, it is the control of illumination coherence that enables to adapt this microscope to various experimental needs, hence the name. Fig. 5 shows a schematic of the CCHM: the light from the source is split into a reference beam (blue) and an object beam (orange). The object beam passes through the studied sample and is directed to the desired output plane (CCD chip). The reference beam is scattered at a diffraction grating and then is inclined towards the object beam. In the output plane, the two beams interfere, and the intensity of the created hologram can be described as:

$$i(x, y) = |o(x, y) + r(x, y)|^2 = |o|^2 + |r|^2 + or^* + o^*r, \quad (4)$$

where  $o(x, y)$  represents the complex amplitude of the object wave,  $r(x, y)$  denotes the complex amplitude of the reference wave and  $o^*$ ,  $r^*$  stand for complex conjugates of complex amplitudes of the object and reference wave, respectively. The first two components of the right side of (4) stand for individual intensities of the object and reference beam and together, they create the zero-order term in the spatial frequency spectrum of the hologram. The two remanent components are denoted as interference terms and carry the information on phase – these terms are used for the complex amplitude reconstruction. [38, 39]

To reconstruct the phase shift and amplitude variation introduced by a studied sample, first, a fast Fourier transform is applied on the yielded hologram. This results in a spectrum of spatial frequencies which form the sample hologram – in the center, there is the zero-order term corresponding to the intensities of reference

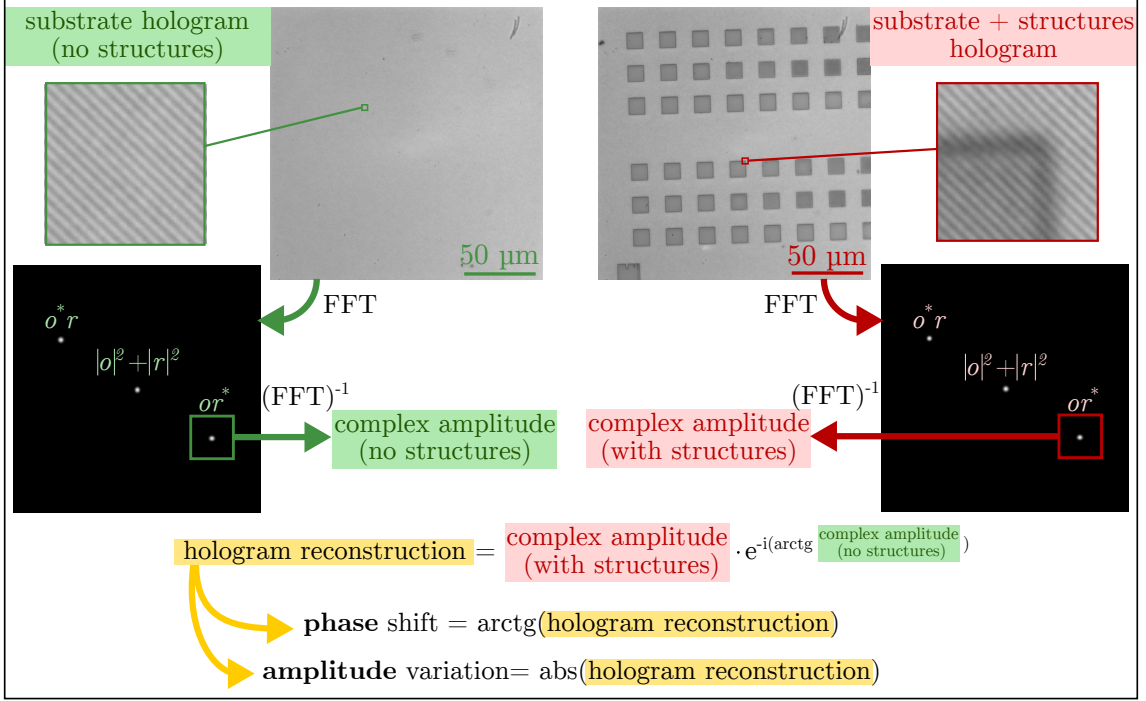


**Figure 6:** Interpretation of CCHM measurements. The holograms obtained with CCHM are first remodeled with fast Fourier transform (FFT). Then, only the spatial frequencies corresponding to the image term  $or^*$  are selected for inverse fast Fourier transform ( $\text{FFT}^{-1}$ ) which then provides the complex amplitude of the yielded image. By the engagement of two such measurements, one for the sample and one for structure-free substrate, the phase shift and amplitude variations introduced by the structures can be established.

and object beams. For phase and amplitude reconstruction, inverse fast Fourier transform is applied on a selected bundle of spatial frequencies corresponding to one of the interference terms  $or^*$  or  $o^*r$ , as marked in Fig. 6. This way, the complex amplitude of the sample is yielded, and the phase shift and amplitude variation introduced by the sample can be determined. Occasionally, the influence of only a specific part of the studied sample on the final phase and amplitude needs to be determined. This can be done in two ways:

- A copy of the studied sample without the specific part can be put in the reference beam, and then, phase and amplitude variation can be retrieved as described afore.
- The reference object slot remains empty and two measurements are carried out, one including the interesting part (e.g. structures) of the sample, the other capturing the sample area without the interesting part. This method is addressed in Fig. 6.

It should be noted that this way, the determined phase shift is always only in the range of a  $2\pi$  interval. For correct interpretation of phase quantification with

CCHM, the phase should be unwrapped, i.e., it should be ensured that all of the integer multiplies of  $2\pi$  are added to the measured phase shift.

## 2.4.2 Optical spectroscopy

To characterize the optical response of a sample, optical spectroscopy analyses the dependence of light intensity on the wavelength of the used light. Particularly, the light that has been reflected by or transmitted through a sample is analyzed in a spectrometer (see Fig. 7) and properties of the sample like reflectivity, transmissivity, emissivity or absorption can be determined.

Fig. 7a shows a schematic of an optical spectrometer usable in both reflection and transmission geometries. The incoming light is focused on the sample and then follows to the spectrometer, e.g., via an optical fiber. The quantity of light which reaches the spectrometer can be controlled with a slit of adjustable width – this way, the light intensity can be set to values which do not saturate the detector. Further, the spectral resolution of the detection is set by the diffraction grating used by the spectrometer: the finer the grating, the better spectral resolution can

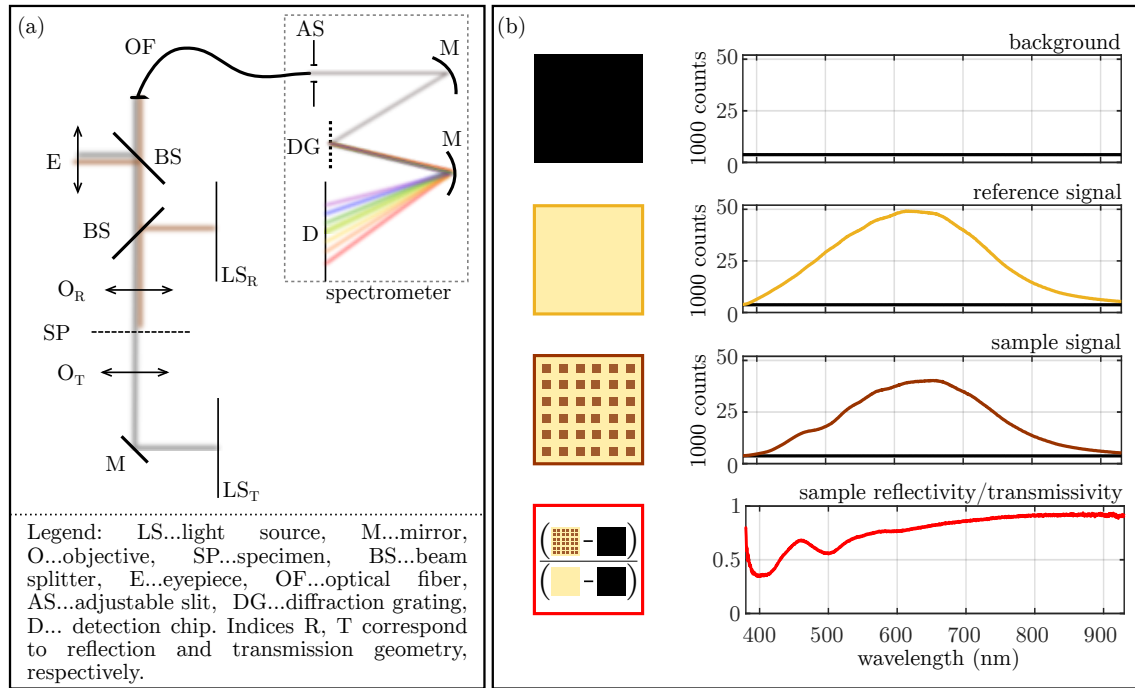


**Figure 7:** Optical spectroscopy. (a) Simplified schematic of an optical spectroscopy setup. An optical fiber is attached to the microscope and directs the light into the spectrometer. Diffraction grating separates the light spatially according to its wavelength – this way, the detector can record the intensity of light with a given spectral resolution. (b) Signal processing for optical spectroscopy: background signal is usually subtracted from reference and sample signals before further processing.

be achieved – however, only limited spectral range can be investigated this way. The diffracted light is naturally splitted across the detection area and hence, the spectral dependence of intensity of the reflected/transmitted light can be determined.

To enable a relevant analysis of the samples with optical spectroscopy, usually two measurements are carried out in order to complete the information obtained by the measurement of the sample. First, the measurement is performed with shuttered light sources (black in Fig. 7b) – the measured signal is then denoted as background and in most cases, it is subtracted from all following measured values. Further, to characterize a specific part of a sample (i.e., metasurface building block array) and exclude the influence of the substrate on the measured optical response, a reference measurement is taken (yellow in Fig. 7b). Depending on the needs of the experiment, reference may be a clear part of the sample (as in without other objects) or an etalon with a well-known optical response, such as gold for reflection or blank volume for transmission. Finally, a spectrum of the sample is measured, as denoted with brown in Fig. 7b. To present the relative optical response of the sample, the sample signal is in most cases divided by the reference signal, as illustrated in Fig. 7b with red.





# 3 METHODS FOR SAMPLE FABRICATION

Fabrication of nano-level metasurfaces is always a process composed of multiple steps. To achieve the desired result, these individual steps can be ordered differently and multiple fabrication strategies can lead to the same outcome. In this chapter, a selection of several important fabrication steps is discussed in detail to provide a theoretical background for the experimental work presented in this thesis.

## 3.1 Thin film deposition of oxides and metals

There are two common approaches to deposit thin layers of materials – chemical depositions and physical depositions. Within this chapter, three examples of particular types of deposition methods will be discussed, first one chemical (atomic layer deposition) and then two physical ones (magnetron sputtering, evaporation). An overview of materials that are commonly deposited by these techniques is presented in table 3.1.

### 3.1.1 Atomic layer deposition

Atomic layer deposition (ALD) belongs to the family of chemical vapor deposition (CVD) techniques, which use chemical reactions occurring on top of the sample surface to create a new layer of material. [40–42] High conformality over any pores or surface roughness and uniformity across large sample areas are key signatures of the CVD techniques. Additionally, atomic layer deposition offers the advantage of repetitive growth of individual monolayers and thus enables depositions of thin films with the accuracy of individual atomic layers [42], see Fig. 8a.

With ALD, an atomic monolayer of a material is formed during a cycle consisting of two alternating steps – one where the sample is exposed to a gaseous substance (often denoted as a precursor) and the other which cleans the reaction chamber

**Table 3.1:** An overview of materials commonly deposited by the selected techniques.

deposition technique	standard deposited materials
ALD	$\text{Al}_2\text{O}_3$ , $\text{HfO}_2$ , $\text{La}_2\text{O}_3$ , $\text{SiO}_2$ , $\text{TiO}_2$
magnetron sputtering	Al, Au, Bi, Co, Cu, Fe, FeRh, Hf, Mo, Nb, Ni, Pd, Pt, Sc, Ta, Ti, $\text{TiO}_2$ , W, Zr, their oxides and combinations
evaporation	Ag, Al, Au, Co, Cr, $\text{Cr}_2\text{O}_3$ , Cu, Fe, Ni, NiFe, NiCr, $\text{SiO}_2$ , Ti, Ta, $\text{VO}_2$ , W

from reaction by-products by pump-down and provides the time needed for chemical reactions to take place on the entire sample surface. Based on the character of the steps which introduce reactants into the deposition chamber, ALD processes can be further divided into thermal ALD and plasma-enhanced ALD. In general, the ALD cycle of both of these methods consists of four steps (see Fig. 8b):

- The sample is exposed to a metal-containing precursor (i.e., base material precursor), either inorganic (e.g., elemental gases and metal halides) or, more commonly, metalorganic gases with functional groups as amides, alkyls, cyclopentadienyls, and others.
- A settling time is allowed so that chemical reactions of the previously purged metal-containing precursor with the substrate can take place on the entire sample surface.
- Thermal ALD: The reaction chamber is purged with a different precursor, which supports the formation of an oxide, nitride, or any other desired chemical compound on the substrate. For depositions of oxides, water vapors or ozone are commonly used; to deposit nitrides and sulfides, ammonia and  $\text{H}_2\text{S}$  are employed, respectively.

Plasma Enhanced ALD: The reaction chamber is filled with gaseous radicals (e.g.,  $\text{O}^*$ ), and plasma is ignited above the sample surface.

- Yet another settling time is held so that the second precursor reacts with the metalorganic compounds on the sample surface.

Since only a single monolayer of the material is formed within each cycle, subsequent repetition of such cycles enables precise control over the thickness of the fabricated layer.

By ALD, a wide variety of materials can be deposited on the sample surface [43, 44]; some of them are mentioned in Tab. 3.1. However, a significant disadvantage of ALD dwells in the low deposition rate. Naturally, this rate differs with individual materials and used precursors. The deposition rate can be moderated by the adjustment of temperature within the reaction chamber. At higher temperatures, chemical reactions will happen at higher rates and the entire surface will be covered faster. Hence, even though the growth rate per cycle is still one monolayer, the duration of the cycle shortens, and the overall growth rate per second increases. However, there are some boundaries which limit the process temperature to the so-called “ALD window”, see Fig. 8c. Namely, if the temperature of the sample surface would be too low (possibly for the preservation of some resist mask), the reactivity of the precursor would either not suffice to the creation of an atomic monolayer on the sample or be so high that clusters of the precursor molecules would be created. On the other hand, if the temperature of the sample surface is too high, the precursor molecules either desorb from the sample or they decompose. [44]

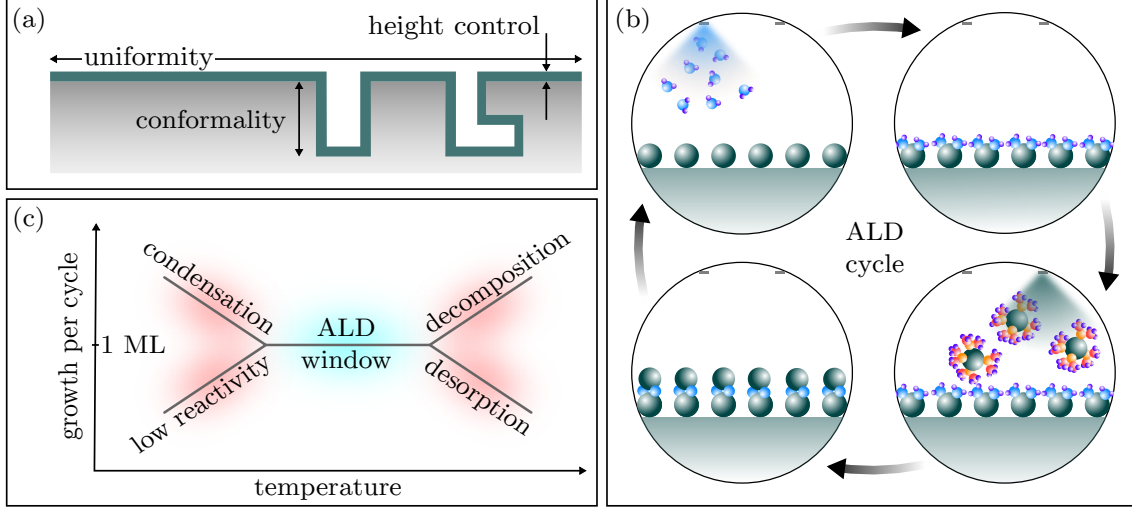


**Figure 8:** Atomic layer deposition. (a) ALD enables the deposition of thin films with high conformality, uniformity and very controlled height. (b) Atomic layer deposition cycle. Steps where individual precursors (blue-violet, teal-orange) are purged into the reaction chamber interlace with steps serving to chemical reaction to take place on the entire sample surface and the removal of excessive reactants (violet, orange). (c) A monolayer of the deposited material is formed only within a specific temperature range – so-called ALD temperature window.

### 3.1.2 Magnetron sputtering

Magnetron sputtering belongs to a class of physical vapor deposition (PVD) techniques. Individual PVD methods differ mostly in the means of how atoms of the deposited material are extracted from the bulk source and sent towards the substrate. Later, in section 3.1.3, we will also introduce another common PVD method, evaporation.

Magnetron sputtering is commonly used for the deposition of elemental metals, alloys, semiconductors, oxides, nitrides, etc. [45], some of which are listed in Tab. 3.1. For the deposition of oxides or nitrides, there are two possibilities: i.e., either to sputter the specific oxide directly ( $\text{TiO}_2$  for instance) or to perform reactive sputtering – to sputter from a metallic target (e.g. Ti) while the reactive gas (e.g.,  $\text{O}_2$ ) is let in the chamber during the deposition in a controlled way.

In contrast to atomic layer deposition, the process of magnetron sputtering can not be separated into individual cycles. Yet, several events characteristic of this method can be distinguished – all of them occurring on multiple locations in different times, but always in the following order:

- An inert gas is let into the vacuum chamber. Mostly, argon or neon are employed due to their relatively high atomic mass, which increases the sputtering yield, i.e., the number of target atoms being sputtered by a single gas

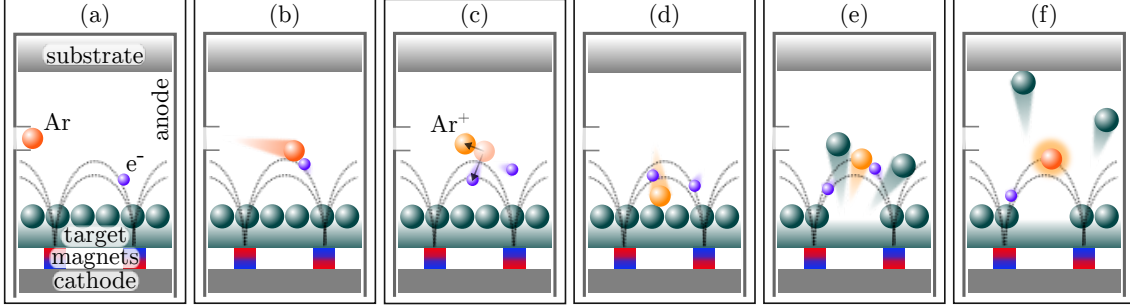


**Figure 9:** Magnetron sputtering. (a) Inert gas is let in the deposition chamber and (b) one of its atoms collides with an electron. (c) The inert gas atom is ionized and (d) drawn towards the target. (e) The target surface is eroded by the cation. The cation and one or more neutral target particles are ejected away from the target. (f) The sputtered particles reach the substrate or chamber walls. Cations may absorb a nearby electron and emit the excessive energy in the form of photons. Inspired by [46], where many other interesting animations describing the events occurring during magnetron sputtering can be found.

atom. The presence of an inert gas increases the pressure inside the vacuum deposition chamber – commonly, a pressure of thousandths of millibar is maintained during the deposition process. Due to the presence of a high voltage bias between the cathode (located behind the target) and the anode (typically the chamber wall), ever-present free electrons are repelled from the cathode. Magnets, located behind the target, manage to contain such electrons in the vicinity of the target (see Fig. 9a).

- The inert gas atom collides with an electron (Fig. 9b) and is ionized – (Fig. 9c).
- The cation is then attracted to the cathode and keeps moving towards the target. Electrons (both the incident and the kicked-out) follow specific paths given by the presence of the electric and magnetic field (Fig. 9d).
- Upon collision of the cation and the target, one or more neutral particles of the sputtered material are ejected from the target. These particles follow a linear trajectory – at best, they reach the substrate. The directionality of the sputtering is low – in many cases, the neutral target particles reach the chamber wall rather than the substrate. The primary cation can either be again drawn back to the target by the electric field force or it might absorb a nearby electron, the latter being illustrated in Fig. 9e,f). During such a process, the excessive energy is emitted in the form of photons – hence, during deposition, the plasma glows. Other electrons remain trapped by the magnetic field in the vicinity of the target rather than striking the newly formed layer on the substrate, thus not lowering the deposition rate.

Within reactive magnetron sputtering, a second gas inlet is present, which can

introduce some additional reactive gas to the deposition chamber ( $\text{O}_2$  for oxides,  $\text{N}_2$  for nitrides). Particles of the sputtered material reach atoms of the reactive gas and together, they land on the substrate. To moderate the stoichiometry of the produced layer, the partial pressure and the flow of the reactive gas must be regulated.

Additionally, the deposition process differs for sputtering of conductive and non-conductive materials. The main difference dwells in the generator used to maintain the voltage bias: for the deposition of conductive materials (a majority of cases), a direct current (DC) source is used, while to deposit non-conductive materials (non-reactive sputtering of oxides, e.g.), a radio-frequency (RF) source is employed. [47] During DC sputtering, the cations of the sputtering gas may accumulate on the surface of the non-conductive target, making it positively charged. Such charge buildup can terminate the discharge of sputtering atoms. RF sputtering solves this issue by alternating the electric potential at radio frequencies. This reverses the charge buildup periodically, leaving the target charge free. The reason why RF sources are not used widely for depositions of both conductive and non-conductive materials is the low growth rate associated with them. Commonly, DC sputtering allows for deposition rates of units of Ångströms per second, while RF sputtering yields only about tenths of such rates.

### 3.1.3 Evaporation

Evaporation is one of the most common representants of the PVD-based processes. Within this technique, the deposited material is heated above its evaporation point and newly formed vapor rises up towards the substrate. On the substrate surface, the gas transforms back to the solid state, and a thin homogeneous layer of the material is built. Two main types of evaporation-based deposition processes are distinguishable: electron beam (e-beam) evaporation and thermal evaporation. [47]

Thermal evaporation uses the electric current flowing through a crucible to heat the target material, as shown in Fig. 10a. This way, the entire volume of the target material is heated. The deposition rate is thus given mostly by the amount of the electric current, which heats the crucible and the material in it.

During e-beam evaporation (see Fig. 10b), the target is heated locally, as electrons formed into a beam strike a small area of the target surface. The electron gun which emits the electrons is located beneath the crucible, safe from being covered by any deposited material. A magnetic field is applied so that the trajectories of the emitted electrons aim towards the target. Electrons follow a characteristic circular trajectory – the size and the position of the beam spot within the crucible are controlled by additional apertures. These parameters, alongside with the amount of the electric current formed by the e-beam, allow for moderation of the deposition rate.

The deposition rate yields highest values when the e-beam is focused into a small spot. However, this may drill a narrow hole throughout the target material which exposes the crucible. This must be avoided and hence, beamspots with reasonable diameters are used in practice and attention is paid to avoid the crossover of the beam spot with the edges of the crucible.

A schematic of an e-beam deposition chamber is shown in Fig. 10c. For e-beam evaporation, there are usually several crucibles attached to a carousel and a single electron source, so the simultaneous deposition of different materials is impossible. Thermal evaporation, on the other hand, offers multiple solutions to this issue. Either several boats, each containing a different material, can be placed in the deposition chamber, or one boat can be filled with a mixture of the desired materials (attention must be paid to temperatures at which individual materials evaporate). Further, a deposition chamber often includes a thickness meter to monitor the deposition rate so that a layer with desired thickness can be produced. For this purpose, a quartz crystal microbalance (QCM) can be used. QCM is a device that can determine a change of mass by sensing a change in the frequency of a quartz crystal resonator. [48] Subsequently, if the area of the resonator and the density of the deposited material are known, one can establish the thickness of the deposited material. Such a device often has its own shutter to be protected from excessive buildup of material on its surface (e.g., when a silver target must be cleaned for

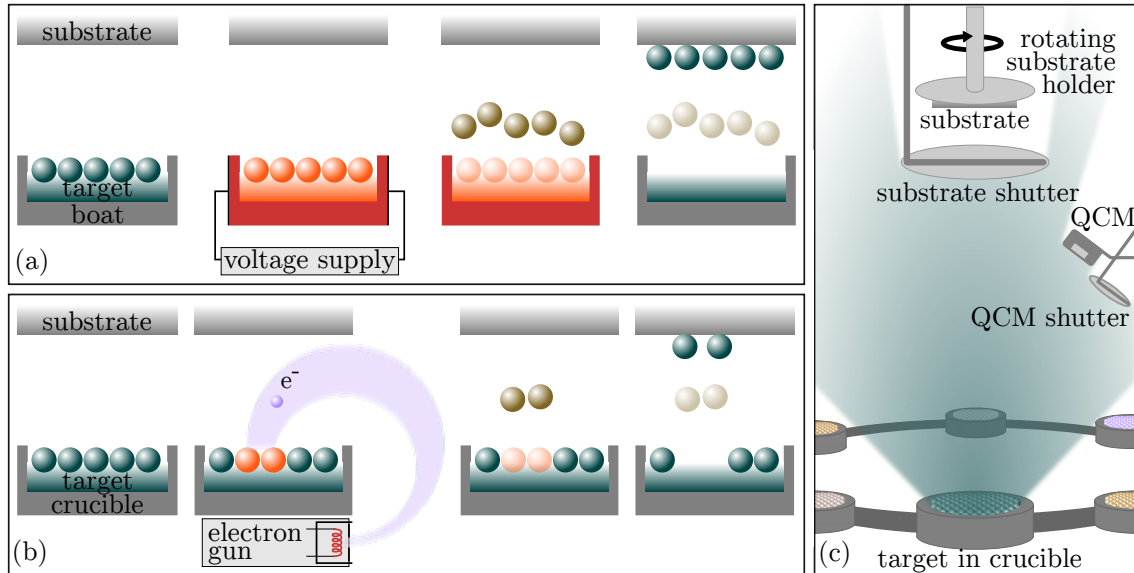


**Figure 10:** Evaporation deposition. (a) Thermal evaporation. The boat and all of the material located in it are heated by the electric current running through the boat. (b) Electron beam evaporation. A beam of electrons locally heats up the target material within a crucible. (c) Important features of an evaporation deposition chamber.

a while before the deposition to remove the surface oxide). For the same reason, the substrate itself is protected by a shutter. To produce layers of high quality, the deposition rate should not change over the course of deposition and hence, the substrate is covered by a shutter also during the time necessary for the deposition rate to stabilize (accuracy to hundredths of Ångströms per second can be achieved). The initial instability of the deposition rate is caused by temporal delays in heating and evaporation of the target material – after some time, the material is heated equally and the deposition rate becomes constant. Typically, deposition rates of evaporation processes are higher than the rates yielded by magnetron sputtering – orders of 0.1-10 Å/s can be achieved.

To maintain the homogeneity of the deposited layers, all of the PVD methods can use the following additions. A rotating substrate holder provides good uniformity of the layer across large areas, units of revolutions per minute are commonly used. The uniformity of the layer can also be enhanced by the relative position and relative tilt of the substrate with respect to the target. The formation of a homogeneous layer can be further achieved by heating of the substrate holder and keeping deposition speed low. The former facilitates the subtle motion of atoms towards ordered structures, whilst the latter provides more time for such motion before any other material is deposited. All of the aforementioned additions need to be calibrated for each individual material in order to achieve perfect results with PVD techniques. On the other hand, CVD-based methods offer excellently deposited layers with significantly lower user effort, but their time consumption often makes them disadvantageous, especially if thicker layers should be produced.

## 3.2 Electron beam lithography

Electron beam (e-beam) lithography is a widely used method for nanostructure fabrication, especially in combination with other techniques. The resulting lithographically fabricated polymer topography on the sample surface can serve as a mask for thin layer deposition, dry etching, local doping of the sample, etc. [49, 50] An overview of individual steps leading to preparation of polymer topography on top of a substrate is shown in Fig. 11.

The most common competitors to this method are focused ion beam processes, optical lithography, and direct laser writing, as they all offer precise positioning and shaping of the desired structures. For the fabrication of metasurfaces, focused ion beam processes turn out to be quite inefficient – the time-consumption of these methods is very high when large areas of the sample should be patterned. Optical lithography, on the other hand, does not suffer from this issue: the exposition of



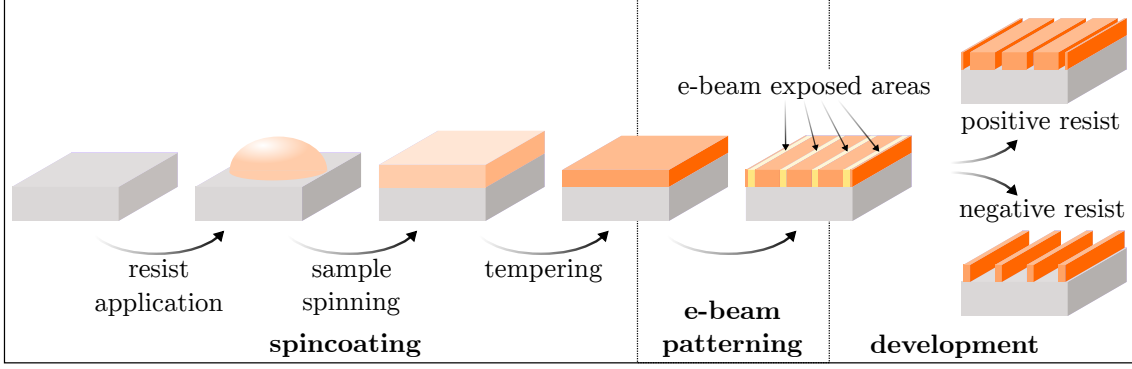


**Figure 11:** Processing steps of electron beam lithography. First, a thin layer of e-beam resist is spincoated on the sample surface. The resist is then locally exposed to a focused electron beam, and after appropriate chemical processing (development) the final polymer topography is produced on the sample surface.

specific patterns is feasible within seconds, as non-transparent masks are placed between the light source and resist-covered sample. This method is advantageous for mass fabrication of identical samples. When a series of different patterns are desired, the preparation of corresponding non-transparent masks gets expensive and time-consuming. Direct laser writing is very similar to e-beam lithography and suits the purpose of metasurface fabrication almost perfectly. However, the lateral resolution of this method reaches hundreds of nanometers at best and thus, fabrication of metasurfaces for optical applications would be challenging. Due to all these reasons, e-beam lithography seems to be the best option for the fabrication of metasurfaces composed of nano-sized structures in the context of research and development. In the following text, this method will be discussed in detail.

### 3.2.1 Spin-coating

The goal of a spin-coating step in e-beam lithography is to prepare a thin layer of e-beam resist on the sample surface for subsequent e-beam patterning. Hence, it is the first step of electron beam lithography.

An e-beam resist is a polymer solution (the solvent being typically anisole, chlorobenzene, toluene, ethyl lactate,...) sensitive to e-beam exposure. Depending on how the e-beam exposure affects the polymer chains within the resist, two resist-types are distinguished: positive and negative e-beam resist. Polymers in positive e-beam resists tend to decompose into shorter polymer chains when exposed to electrons – this leads to increased solubility in the affected part of the resist. On the other hand, the polymer chains in negative e-beam resists interlock each other upon e-beam irradiation, causing a decrease of polymer solubility when compared with the unaffected polymer volume, as denoted in Fig. 11. [51]



The preparation of a thin e-beam resist layer starts when a droplet of the resist is placed on the sample surface. Typically, for a sample of  $(1 \times 1) \text{ cm}^2$ ,  $(40 - 70) \text{ }\mu\text{l}$  of the resist is needed. The sample is then spun at high frequency – this forces the applied resist to spread across the sample surface due to centrifugal forces acting on the resist. Finally, a thin layer is formed on top of the sample. The thickness of the produced layer depends mostly on two factors: the frequency of the spinning and the density of the resist, the latter being given by the solvent type and polymer concentration. In general, polymer layers produced by more concentrated resists are thicker. To decrease the thickness of the produced resist layer, a high frequency is used for the sample spinning. In technical practice, information about the final layer thickness as a function of the sample spinning frequency is enlisted in datasheets of individual resists.

E-beam resists in general do not easily stick to the surface of the sample. In some cases, the adhesion between the e-beam resist and the sample surface needs to be enhanced. This can be achieved by plasma cleaning of the sample surface or by application of an organosilane based adhesion promoter, such as hexamethyldisilazane (HDMS) atmosphere or diphenylsilanediol solution (AR 300-80). Plasma cleaning of the sample aims towards creation of a shallow topography on the sample surface. This serves as a physical barrier when the resist spreads across the sample surface and the resist is prevented from falling down of the spinning sample surface. Alternatively, the enhanced adhesion of the resist to the sample can be achieved chemically, by exposing the sample to an HDMS atmosphere or by applying AR300-80 on the sample surface via spin-coating. These adhesion promoters consist of silicon central atoms and organofunctional groups. The former bind well to oxygen atoms of the oxidized sample surface, the latter support the reactivity between the adhesion promoter and the resist. [52]

The thin resist layer produced by the spin-coating method still contains a lot of the solvent fluid. This can be removed from the sample surface by additional heating of the sample to the temperature above the evaporation point of the solvent for several minutes. For common solvents, the tempering temperatures reach around  $(130 - 180)^\circ\text{C}$  and the tempering is feasible with the use of a hotplate for direct heating of the sample.

After tempering, the prepared resist layer is ready to be patterned with an electron beam. However, if the underlying substrate is non-conductive, an additional conductive layer must be spin-coated/deposited on the sample as well, to support discharging of the electrical charges which are generated during electron beam exposure. Typically, these layers are from conductive polymers or metals such as aluminum, chromium, titanium, or even silver. It should be noted that after patterning, these conductive layers must be removed before the resist development.

### 3.2.2 Patterning with an electron beam

Resist patterning with electron beam lithography requires three supporting systems: a design of the pattern, a focused electron beam, and a lithographic stage with an accurate positioning system.

The design of the pattern is in a majority of cases a binary image which determines, which areas of the sample are supposed to be irradiated by the beam. Alternatively, greyscale lithography enables to alter the polymer topography gradually. [53, 54] If the design includes various types of structures (e.g., large and small), it might be advantageous to perform the patterning of individual structure types under different conditions (beam current, dose,...). Hence, the design can be composed of several layers and each layer can be processed individually during the electron beam patterning.

The focused beam of electrons is created in the so-called electron column [55]. The generated electrons are accelerated by the applied voltage bias (up to 30 or 100 kV) and formed into a neat beam by apertures and magnetic lenses. To ensure that the beam spot is as small as possible (so that the design is patterned with high resolution), it is essential to align the electron beam and to minimize the stigmatic aberrations for the desired working distance, acceleration voltage and beam current. For these purposes, every exposition of a new sample requires its own, iterative adjustments of electron beam centering, stigmators and working distance. The size of a writefield depends on the used working distance and magnification – for lithography, it commonly varies from 1 to 1000  $\mu\text{m}$ , and is related to the exposition design as well. Large writefields are used when the patterned structures are somewhat large, too, e.g. paths to electrical contacts. For fine structuring at the scale of tens of nanometers, small writefields are used. Often, especially with metasurfaces, fine structuring of the resist is required in areas larger than the writefield. To overcome this issue, special lithographic stages are used.

A lithographic stage enables a very precise motion of a sample under the electron beam. The beam is thus able to pattern any area of a sample without being much deflected, which prevents the beam spot from the most significant defects. Before the patterning of each new sample, it is necessary to align coordinate systems of the design, the sample and the lithographic stage. This includes selection of the origin on the sample, rotation correction between the sample position and the design, focusing correction so that any part of the sample is treated with appropriate working distance and finally, writefield alignment. [56] If these arrangements are done correctly, it is possible to stitch multiple writefields with high accuracy (up to 5 nm) and ensure high-resolution patterning over large areas ( $\sim \text{cm}^2$ ).

Finally, each type and thickness of an electron resist requires a different dose of

electrons so that its polymer structure is altered in a sufficient manner. This dose can be expressed as following:

$$\text{area dose (C/m}^2\text{)} = \frac{\text{beam current (A)} \times \text{dwell time (s)}}{[(\text{step size (m)})]^2}, \quad (5)$$

where the beam current (common values  $10^{-11}$ - $10^{-9}$  A) can be measured with a Faraday cell, the dwell time or the step size can be arbitrary and the other of the two is calculated for a desired area dose. The step size denotes the length by which the beam is moved to new locations (usually units of nanometers for fine patterning with small writefields, but tens of nanometers for large beam currents) and the dwell time determines, how long is the beam still at each location. Although there usually is a recommended dose for a given resist thickness in the resist's datasheet, it is advantageous to perform a test of various doses for any new task before the final exposition.

### 3.2.3 Resist development

After the electron beam alters the polymer structure of the resist, the sample must be further processed in order to reveal an actual topography on its surface. During resist development, the exposed (or not exposed) parts of the positive (negative) resist are dissolved faster than the rest of the resist due to the change of solubility caused by alternated polymer structure. [52] This process should be done shortly after the patterning – otherwise, the internal structure of the polymer could begin to change to its original form, thus devouring the final topography by making the previous e-beam patterning useless. To develop the resist, the whole sample is submerged in a solvent (developer) for a certain amount of time. To achieve perfect topography after the development, an appropriate combination of the development time and the area patterning dose needs to be engineered with respect to the used resist and its thickness. Note that, even after a sample is pulled out from the developer, the residual fluid keeps dissolving the resist layer. Hence, it is necessary to terminate this process by placing the sample into a substance, denoted as stopper, which dilutes the developer and finally, drying the sample from the stopper fluid. After this step, the desired topography should be imprinted into the resist.

## 3.3 Etching

Etching is a chemical and/or physical process, which aims to alter the material surface either via dissolution in a chemically active environment and/or exposition to high-energy particles, respectively. Etching processes can be further distinguished

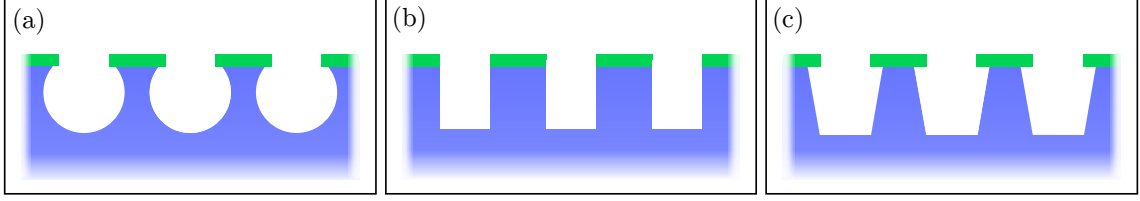


**Figure 12:** Profiles achieved by different etching methods. (a) Chemical, wet isotropic etching. (b) Physical, dry anisotropic etching. (c) Wet anisotropic etching – material with a preferential crystallographic orientation is etched faster.

by the etching substance itself — etching with liquid substances is denoted as wet, whereas etching with gases or a plasma is referred to as dry. [57] To characterize the nature of an etching process, several factors can be considered: etching speed, its variation towards different materials (selectivity), and its spatial variations (isotropy), too. The selectivity of an etching process determines how much faster is one material etched in comparison to the other. This quantity is often used in selective etching, where a mask is put on top of the sample surface in order to protect some of its parts from etching. In such cases, the mask should be etched slower than the actual etched surface. In other words, the selectivity of such a process:

$$\text{selectivity} = \frac{\text{etch rate of the etched material}}{\text{etch rate of the masking material}} \quad (6)$$

should be larger than one if possible. The directionality of the etching speed divides the etching processes into isotropic and anisotropic. Commonly, chemical etching shows low directionality, thus is isotropic, while physical etching is more directional and tends to have an anisotropic character (see Fig. 12a,b). However, the nature of the directionality of an etching process may change for crystalline matter — the etch rate may vary for different crystallographic orientations of a material, as illustrated in Fig. 12c.

In the following, two etching techniques which find use in the preparation of high-aspect ratio metasurfaces will be introduced: wet etching and reactive ion etching.

### 3.3.1 Wet etching

Wet etching is a purely chemical process, which means that the material is gradually etched due to its presence in a chemically active fluid — an etchant. The reactions occurring at the sample surface deplete the surface of its atoms and thus, the surface is etched. However, the products of these chemical reactions should not remain on the surface of the sample — a passivation layer could be formed, which would prevent the sample from being etched further. [58] To ensure continuity of the etching, usually only such etchants which act as a solvent for the etching products

are used. Further, the separation of the reaction products from the sample surface can be supported by performing the etching in an ultrasound bath. Once a desired amount of material is etched away, the etching process must be stopped. A common way to do so is to relocate the sample into another fluid, which would dilute the etchant remaining on the sample surface. Typically, etchants used for wet etching are water solutions of acids or hydroxides — a few wet etching strategies for selected materials are listed in Tab. 3.2.

### 3.3.2 Reactive ion etching

Reactive ion etching (RIE) combines etching by chemically active gases and sputtering by high-energy ions, thus belongs to the family of dry etching techniques. In this process, the sample is located in a reaction chamber filled with one or more etching gases. A radiofrequency source induces decomposition of the etching gas molecules into ions, which react with the surface of the sample. Similarly to wet etching, the products of chemical reactions should ideally not stay on the sample surface. Because of this, the etching process is often designed in such a way that the reaction products are volatile.

So far, only the chemical etching part of the process was described. The physical part of the reactive ion etching dwells in sputtering of the sample surface by inert gas ions (e.g.  $\text{Ar}^+$ ). In general, this enhances the etch rates of the chemical etching by plasma and adds somewhat directionality to the etching process. [59] For every application, a balance needs to be found between the two etching approaches to achieve the desired speed and isotropy by precise control of the amount of reaction and sputtering gases. Depending on the available etching gases, reactive ion etching can be used to etch metals, oxides, nitrides on other substances, some of them being listed in Tab. 3.2.

**Table 3.2:** Etchants used in etching of selected materials via wet etching and reactive ion etching.

etched material	wet etching	reactive ion etching
Si	$\text{KOH}$ , $\text{N}(\text{CH}_3)_4^+\text{OH}^-$ , $\text{HNO}_3+\text{HF}$	$\text{CHF}_3$ , $\text{SF}_6$
$\text{SiO}_2$	$\text{HF}$ , BOE (buffered oxid etch)	$\text{SF}_6$
$\text{SiN}$	$\text{H}_3\text{PO}_4$	$\text{CHF}_3$
$\text{TiO}_2$	$\text{H}_3\text{PO}_4+\text{H}_2\text{O}_2$	$\text{CHF}_3$ , $\text{SF}_6$
Au	$\text{HCl}+\text{HNO}_3$ , $\text{KI}+\text{I}_2$	-
Cr	$(\text{NH}_4)_2\text{Ce}(\text{NO}_3)_6$ , $\text{HCl}$	-
organics	$\text{H}_2\text{SO}_4+\text{H}_2\text{O}_2$ , acetone	$\text{O}_2$



## 4 RESULTS

To fabricate dielectric nanostructures with high aspect ratio, two strategies have been considered: one employing reactive ion etching (RIE, see section 3.3.2) of a thick dielectric layer through a metallic mask (Fig. 13b), the other relying on atomic layer deposition (ALD, see section 3.1.1) of a desired dielectric into a pre-patterned resist mold (Fig. 13c). As the latter method consists of fewer fabrication steps, one may think of it as of an easier option. However, other factors, such as the time-consumption of individual fabrication steps, accessibility of the needed instrumentation, etc., significantly influence the feasibility of the individual fabrication strategies. Because of this, the seemingly more complicated fabrication strategy was performed entirely while the other is yet unfinished. The stumbling block of the ALD fabrication strategy shown in Fig. 13c was the need to pattern of a thick resist layer which would serve as the mold for ALD. This is feasible only with a lithographic tool with very high-energy electrons (about 80-100 keV) and at the moment, the lithographic tools owned by BUT perform with electrons accelerated by maximally 30 kV. Hence, the help of the Institute of Scientific Instruments (Czech Academy of Sciences) was requested. Outcomes tied to this fabrication strategy are included in section 4.1.1 – even though the fabrication process was not completed,

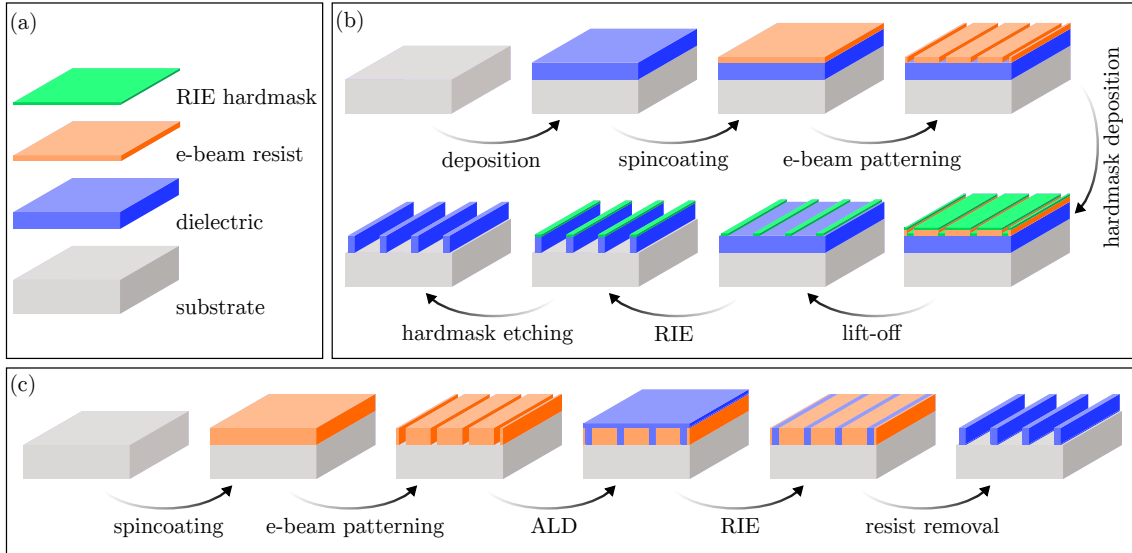


**Figure 13:** Strategies for fabrication of high aspect ratio dielectric nanostructures. (a) Description of used layers and materials. (b) Dielectric material is deposited onto a substrate and is shaped by reactive ion etching through a hardmask prepared by electron beam lithography. (c) Dielectric material is deposited by atomic layer deposition into a pre-patterned e-beam resist mold and then etched by reactive ion etching to the desired height. The final structures are revealed after the removal of the e-beam resist.

the achieved results may be used in further work on metasurfaces at BUT. The following text focuses on the RIE fabrication strategy, which was fully feasible with the instrumentation on CEITEC Nano research infrastructure. Along with the detailed presentation of this fabrication strategy, attention will be brought to the optimization of this fabrication process. Finally, the results of optical characterization of prepared metasurfaces will be addressed at the end of this chapter.

## 4.1 Sample fabrication

The metasurfaces were fabricated on 300  $\mu\text{m}$  thick fused silica substrates. This material was chosen as it is transparent in the visible range and thus suitable for optical applications. First, a 600 nm thick layer of  $\text{TiO}_2$  was deposited on the fused silica wafer by the magnetron sputtering system from BESTEC. During the deposition, the sample was attached to a rotating holder heated to 110  $^\circ\text{C}$ , as such conditions support creation of an even, uniform material layer. To deposit the  $\text{TiO}_2$  layer, a non-conductive  $\text{TiO}_2$  target and radiofrequency source were used. This was favored over the deposition from a Ti target with oxygen gas inlet and direct current source, as such option requires intense optimization to achieve the desired stoichiometry of the material due to an increased number of variable settings. [60] Prior to the deposition, the deposition chamber was filled with argon (20 sccm) and the plasma was ignited under the pressure of  $5 \cdot 10^{-2}$  mbar by a turning the power of the RF source to 30 W. Later, during the deposition, the power of the RF source was elevated to 150 W, the pressure in the deposition chamber was lowered to ca.  $6 \cdot 10^{-3}$  mbar and the argon gas flow was finally set to 25 sccm. Unfortunately, during all of the performed deposition processes, the plasma was not once stable and for short moments, a majority of the power from the RF source was reflected, not forwarded: hence, performed deposition processes and their sputtering rates were not stable. Due to this, only a rough estimation of the deposition rate for  $\text{TiO}_2$  under these conditions is presented, namely (0.11–0.14)  $\text{\AA}/\text{s}$ . The height of the deposited film was determined by stylus profilometry of a trench created on the wafer by applying a bit of kapton tape, which served as a primitive deposition mask. A Bruker Dektak XT profilometer was used for this and all the following profilometry measurements.

Quality of the deposited  $\text{TiO}_2$  film was tested with photoelectron spectroscopy system Axis Supra from Kratos Analytical. First, an overview spectrum was measured to establish which elements are present on the sample surface – see Fig. 14a. Apart from the expected peaks of oxygen and titanium, carbon and silicon residuals were found, too. The presence of carbon contamination on sample surfaces is com-



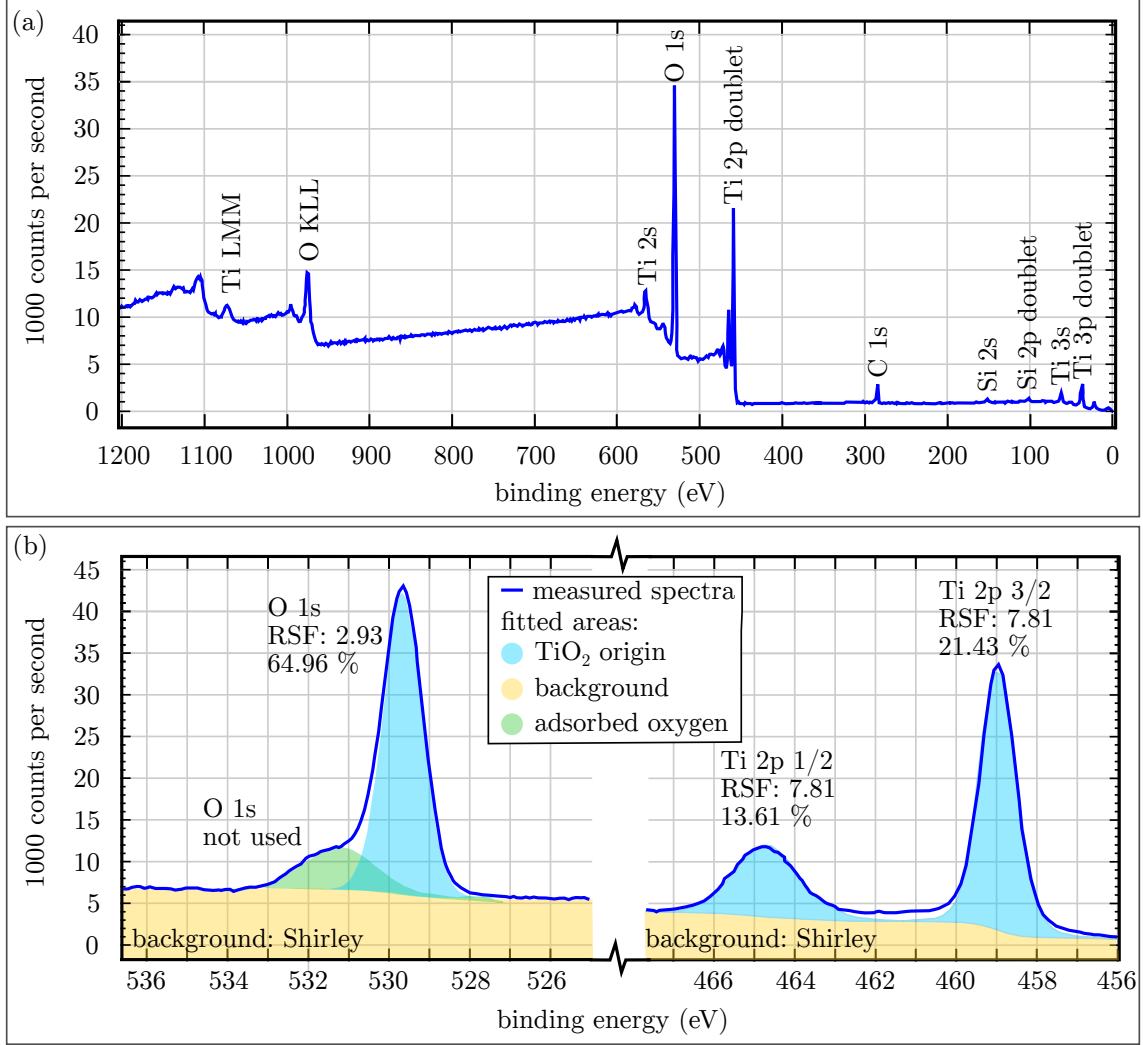


**Figure 14:** X-ray photoelectron spectra of the  $\text{TiO}_2$  layer deposited with magnetron sputtering. (a) Wide spectrum, aside from the presence of titanium and oxygen, carbon and silicon are present too. The former originates from organic residuals the latter most likely from the fused silica substrate. (b) Detailed spectra around the relevant oxygen and titanium spectral lines — quantitative analysis of the measured data shows that deposited layer consists of 65 % oxygen and 35 % titanium.

mon and has already been analyzed, e.g. in [60,61]. Most likely, the measured silicon peaks origin from the fused silica substrate. For the subsequent quantitative material analysis, only narrow spectra corresponding to the O 1s peak and Ti 2p doublet were further measured. In the quantitative analysis (see Fig. 14b), selected titanium and oxygen peaks were fitted by a superposition of a background signal (yellow) and characteristic peaks corresponding to titanium dioxide (blue). The remaining part of the O 1s doublet (green) is considered to originate in the fused silica substrate residuals and hence, was not used in the stoichiometry calculations. The used rel-

ative sensitivity factor (RSF) values were adapted from the library of the analysis tool CasaXPS and denote, how much more likely is the detection of electrons of a given peak than those of C 1s. The obtained data confirm that the deposited layer is composed of ca. 65 % oxygen and 35 % titanium, which corresponds to  $\text{Ti}_1\text{O}_{1.85}$  stoichiometry. Such deviation from the desired stoichiometry is acceptable for the future purpose of the metasurface and could be contingently improved by allowing some oxygen gas into the magnetron deposition chamber during the deposition.

The wafer covered by the titanium dioxide layer was then diced with Oxford Laser A-Series laser cutter. To protect the deposited  $\text{TiO}_2$  layer from undesired damage during the wafer cutting, a thick layer of polymethylmethacrylate was spin-coated on top of it, and the wafer was heated up to  $180^\circ\text{C}$  so that the polymer layer hardens. The wafer was then cut by the laser dicer into small parts. Further, these parts were pre-sectioned (cut halfway only) into several individual samples of  $(8 \times 8)\text{mm}^2$  size, to be broken apart later in the fabrication process. Such an approach facilitates (or even improves) some of the primary fabrication procedures:

- One large piece of the substrate is spin-coated rather than several small pieces. In the spin-coating process, the edges of the sample often suffer from bad resist coverage – a greater amount of resist is located on them than in the central part of the sample. This issue is now overcome and only several samples (from the edges of the wafer piece) eventually suffer from uneven resist coverage.
- The patterning with an electron beam is carried out in a single run for multiple samples. Hence, less time must be spent by adjustments and alignments of the lithographic tool. Furthermore, the produced samples are patterned under the same conditions – the patterns on individual samples can be thus considered identical.
- The development time is identical for all the patterned structures, which further supports the equality of the produced samples. This aspect is important for the optimization of the fabrication process – namely, all of the differences in the quality of multiple samples can be directly tied to a specific process that was performed after sample development. Such a process can be then modified in various ways and the results of individual process modifications can be compared easily.

After laser cutting, the pre-sectioned wafer parts were cleaned in a process composed of five steps. First, an ultrasound acetone bath was performed in order to remove organic residuals from the sample surface. The resist layer which protected the wafer during laser cutting was removed in this step, too. Secondly, an ultrasound isopropyl alcohol bath was performed so that the residual acetone is removed. Further, the samples were cleaned in an ultrasound deionized water bath in order to dilute the residual isopropyl alcohol. Each of these steps lasted five minutes to

ensure complete removal of impurities from the sample surface. Finally, to remove the water from the sample surface, the samples were blown with nitrogen gun and then they were heated to 150 °C with an electric hotplate for 5 minutes.

After sample cleaning, a thin layer of positive e-beam resist CSAR 6200.09 was spin-coated on top of it. However, as the prior experiments have shown that the adhesion of this resist to the TiO<sub>2</sub> surface is poor, various techniques were probed to improve this situation (see discussion in section 3.2.1). Expositions of the sample to both HDMS atmosphere and plasma cleaning have proved to be inefficient. Hence, a thin layer of adhesion promoter AR300-80 was spin-coated on the TiO<sub>2</sub> surface at 4000 rpm, with acceleration 2000 rpm/s for 60 s and later, the sample was baked at 150 °C for 1 minute to allow the promoter to harden, as stated in [62]. This layer enabled good adhesion of the e-beam resist which was then applied onto the sample at 4000 rpm with acceleration 2000 rpm/s for 60 s to create a ca. 200 nm thick layer. [63] Afterwards, the sample was kept at 180 °C for three minutes to harden the resist. As the used substrate and titanium dioxide are both non-conductive, a layer of conductive polymer (Electra 5090.02) was spin-coated on the top of the samples to prevent them from charging during the e-beam patterning. According to the product datasheet [64], spin-coating of this substance at 4000 rpm for 60 s should result into a layer of 140 nm thickness. Finally, this layer was allowed to set during the sample baking at 180 °C for 3 minutes on an electric hotplate. The final order of individual sample layers is shown in Fig. 15a.

For e-beam patterning, the scanning electron microscope Mira3 (TESCAN) with lithographic stage system from RAITH was used. The acceleration voltage of the electrons in the beam was 30 kV and the beam carried the current of 25 pA. For a working distance of ca. 9 mm, the beam was adjusted and aligned to operate well in a writefield area of (50 × 50) μm<sup>2</sup>. To fabricate the test sample, geometries from Fig. 15b were used for various characteristic dimension values, as denoted in Fig. 15c. Patterning doses varying from 100 to 190 μC/cm<sup>2</sup> were used – with a step size of 5 nm, the dwell time ranged between 1 and 2 microseconds. The following analysis of the fabricated structures has proved that each of the design types (ideally, with respect to characteristic dimensions, too) requires a different dose. This is a natural cause of the proximity effect – since all of the proposed patterns are dense, the electron beam affects the structures in the proximity of the currently patterned structure as well. Because the planned metasurfaces combine structures of various sizes in relatively small areas, the best way for an accurate patterning would be to employ a proximity effect correction. [65] In such correction, the electron beam area dose in each patterning point is recalculated so that overall, the designed areas are exposed with a given dose of electrons. In practice, the variations in the area dose are achieved by altering the dwell time in each of the patterning spots. However,

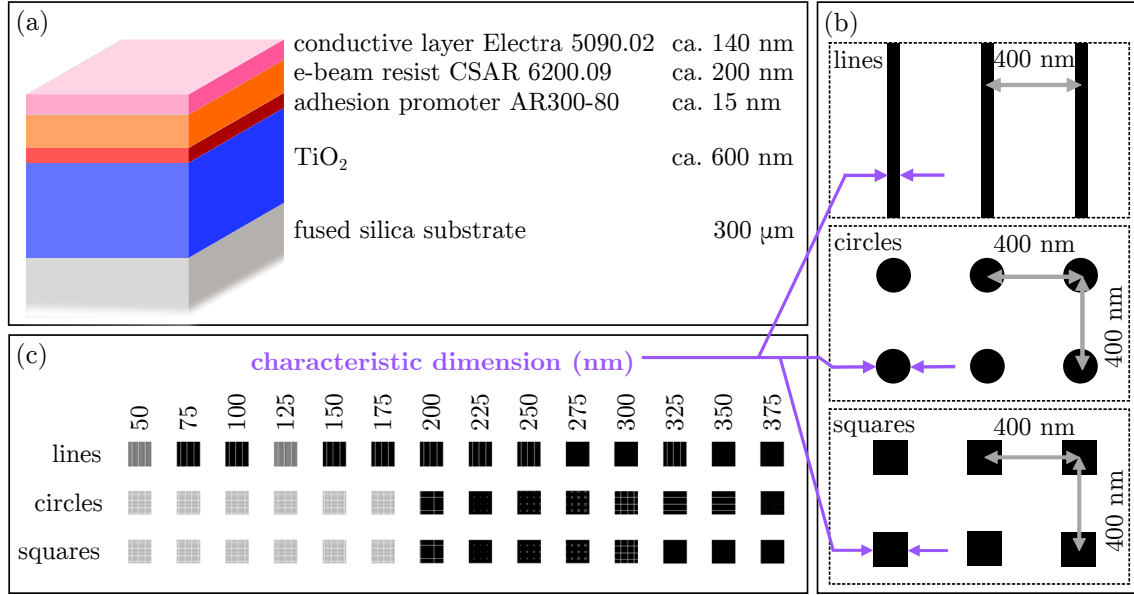


**Figure 15:** Sample patterning. (a) Schematic of the sample layers before patterning. (b) Geometry of the three design motives used for patterning: for lines, circles and squares, the characteristic dimensions are marked with purple. (c) Overview of the design of the test samples. For each geometrical motive, a variety of characteristic dimension values has been used. This pattern was reprinted on the sample several times, each time with different electron beam area dose.

preparation and execution of such correction for large fields with large number of structures are challenging and doing so significantly extends the fabrication time. Therefore, the proximity effect correction was not used for the fabrication of the presented test samples.

Prior to resist development, the conductive layer was removed from the top of the sample by submersion in deionized water for 60 s. Then, the samples were dipped in CSAR developer, which supported the dissolution of exposed resist areas. The developing process was allowed for 60 s and afterwards, it was terminated as the samples were submerged in isopropyl alcohol for 30 s. In this manner, a resist mask for the deposition of chromium was prepared on top of the titanium dioxide layer.

The chromium layer was deposited onto the sample via e-beam induced evaporation (see section 3.1.3) by electron e-beam evaporator from BESTEC. The samples were attached to a rotating holder during the deposition. The chrome target was locally heated by an electron beam of current 16 mA and a deposition rate of 0.8 Å/s was used to deposit 80 nm thick layer of chromium. To enable removal of excessive metal and the resist mask, the samples were submerged into acetone overnight (ca. 14 hours). Afterwards, the beaker with the acetone was put in an ultrasound bath for 60 seconds — doing so facilitates the detachment of the excessive metal

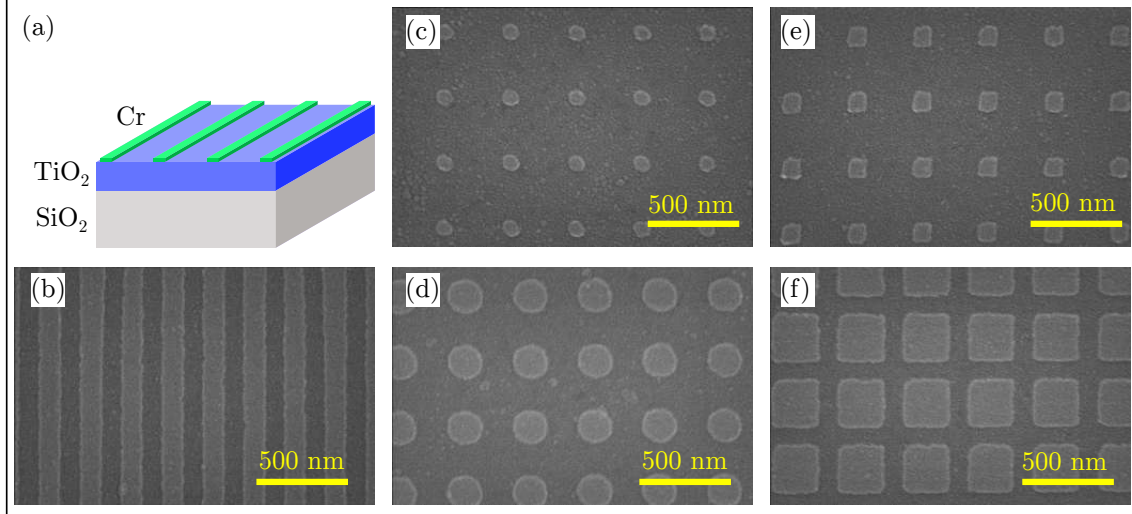


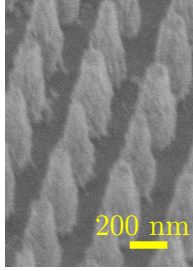
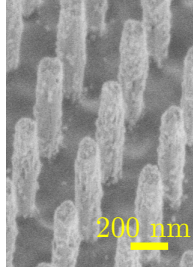
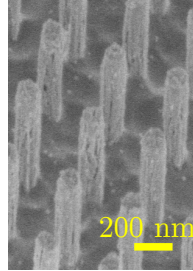
**Figure 16:** Scanning electron microscopy of chrome hardmasks for reactive ion etching. (a) A schematic of the samples shown in (b)-(f). (b) Chrome mask of the line motive with characteristic dimension 125 nm. (c-d) Chrome masks of the circle motive with characteristic dimensions 75 nm, 175 nm, respectively. (e-f) Chrome masks of the square motive with characteristic dimensions 100 nm, 250 nm, respectively.

from the edges of desired structures.

At this stage, the pre-sectioned wafer piece was intentionally broken into several small samples. The quality of the produced chromium mask was tested first by measuring the thickness of the chromium mask layer using a mechanical profilometer. Furthermore, the quality of the produced hardmask was examined with scanning electron microscopy, Verios 460L (ThermoFisher Scientific) was used. The observation of these structures was somewhat challenging due to the non-conductive character of the samples. As the studied sample was supposed to remain functional for further fabrication steps, it was impractical to deposit a thin conductive layer on the top of the sample. Instead, each sample was attached to a metallic stub with four copper tape pieces (one for each of the sample edges) and the images of the hardmasks (presented in Fig. 16) were obtained by the use of 2 kV acceleration voltage and 13 pA of current in the scanning beam to minimize the possible charging of the sample. However, low acceleration voltage causes the interaction volume of the sample to be small and because of that, only a few secondary electrons are detected per a time unit. Therefore, the presented images were taken with relatively high scanning speed and multiple (8 or 16) frames were averaged for one micrograph to reduce the image noise.

After chromium mask quality inspection, the prepared samples were individually modified by reactive ion etching (see section 3.3.2). The chemical part of the etching was supported by the presence of  $\text{CHF}_3$  (30 sccm) and oxygen (1–5 sccm), whilst

**Table 4.1:** Comparison of results achieved by reactive ion etching with different oxygen supply in the reactive gas mixture. The inset images are micrographs of the resulting structures taken with scanning electron microscopy under 40° tilt.

<b>O<sub>2</sub> supply</b>		<b>1 sccm</b>	<b>3 sccm</b>	<b>5 sccm</b>
etch rate TiO <sub>2</sub>	(nm/s)	0.344	0.333	0.322
etch rate Cr	(nm/s)	0.011	0.016	0.038
selectivity	(-)	31	20	8.3
height	(nm)	600	600	600
top/base diameter	(nm)	95/170	100/130	100/120
aspect ratio	(-)	3.5:1	4.6:1	5:1
side wall effect				

the physical part of RIE was carried out in Ar atmosphere (50 sccm). The pressure inside the etching chamber was maintained at 50 mbar and the power of the electric source was set to 200 W. After reactive ion etching, the created topography was briefly examined with stylus profilometry, see further discussion below.

Then, the remaining hardmask material was etched away chemically (see section 3.3.1). The samples were submerged in chrome etchant TechniEtch Cr01 from Microchemicals for 20 minutes – such a long time was probably not necessary, but since this etchant is often re-used multiple times in the laboratory, the original etch rate could be no longer guaranteed. To stop the etching process, the sample was submerged into deionized water for 60 s. Then, the deionized water was reloaded and submersion of the sample continued for another 60 s. The double water bath assures complete dissolution of the etchant and cleans the sample from any remanent etchant. The samples were dried with nitrogen gun and electrical hotplate in a standard way. Finally, the topography of the samples was examined once again with stylus profilometry.

The differences in the sample topography profiles before and after both etching processes enabled analysis of the reactive ion etching etch rate. Inspired by Ref. [66], the effect of different oxygen flow rate was studied. The comparison of results achieved with oxygen supply of (1, 3 and 5) sccm is presented in Tab. 4.1. Along with variation in the etching rates, the resulting profiles of individual metasurface building blocks change too. This clearly shows the importance of proper balance



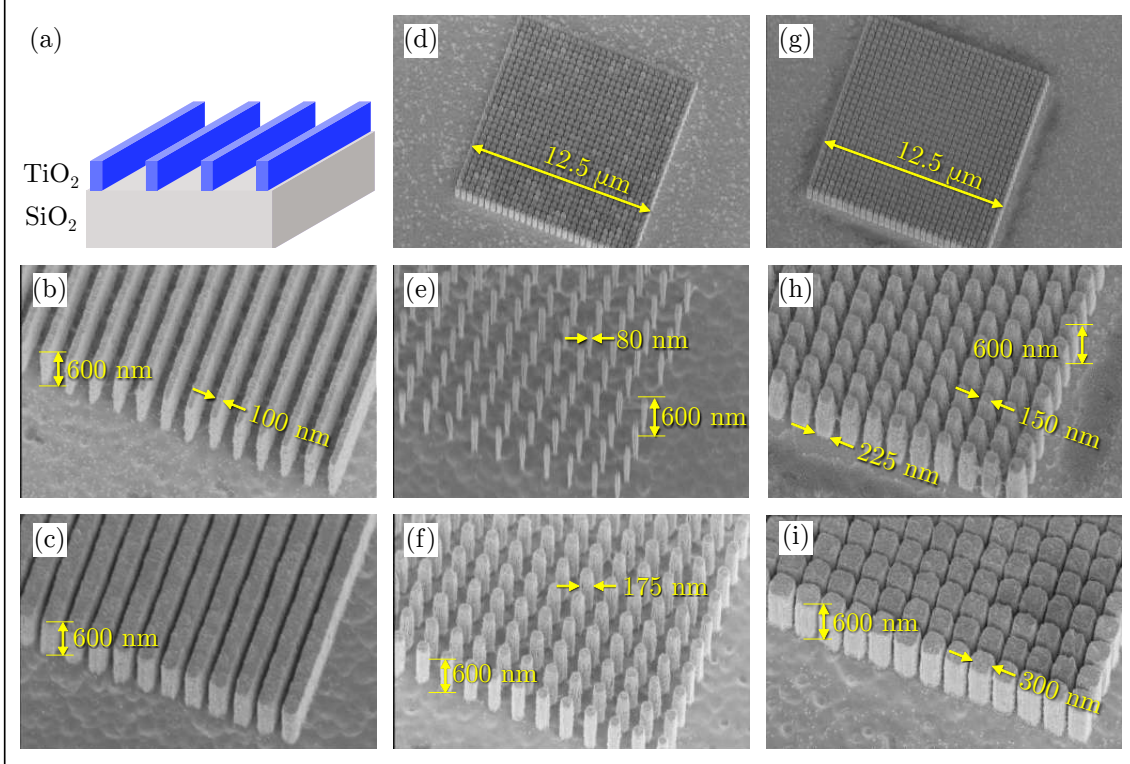


**Figure 17:** Scanning electron microscopy of the final structures. (a) Schematic of the shown samples. (b-c) Final wall-like structures for the polarization waveplate. (d-f) Final building blocks with circular base and (g-i) square base for the phase shifting surfaces used in diffractive beam splitters.

between the chemical and physical etching, which are combined in a RIE process (see discussion in 3.3.2).

Finally, the produced samples with high-aspect ratio  $\text{TiO}_2$  nanostructures were observed via scanning electron microscopy, again with Verios 460L (ThermoFisher Scientific). Yet again, coating of the fabricated samples with a thin conductive layer to prevent the sample from charging was not an option – the high aspect ratio structures could easily break free from the substrate during removal of the used conductive layer. Hence, the samples were treated in the same way as before: they were attached to the sample holder with copper tape, low voltage and beam current were used for imaging, and the micrographs were assembled from the average of multiple images. Additionally, the sample was tilted by  $40^\circ$  from the scanning electron beam so that the three-dimensional character of the structures could be observed. Fig. 17 shows some of the fabricated structures, which were further optically characterized (see section 4.2).

#### 4.1.1 Other fabrication results

The following text will summarize the results achieved with the fabrication strategy proposed in Fig. 13c. The presented outcomes were achieved upon collaboration with the Institute of Scientific Instruments of the Czech Academy of Sciences (ISI CAS).

A 3-inch fused silica wafer of 300  $\mu\text{m}$  thickness was sent to ISI CAS, as the proposed fabrication strategy required to create a 600 nm thick patterned resist mold and was not feasible independently at CEITEC Nano RI. At ISI CAS, the wafer was covered with the e-beam resist CSAR 6200 and then patterned with a lithographic tool operating at 80 keV in a manner described in Fig. 18.

All of the following steps of the fabrication process were performed by the author at CEITEC Nano RI. First, the received wafer covered with the resist mold was cut into individual samples. The next step of the proposed fabrication strategy was the deposition of a dielectric layer into the resist mold was with atomic layer deposition. With respect to the design of the proposed building blocks, a layer of 150 nm thickness should be deposited into the mold so that all of the prepared holes would be fully filled. In atomic layer deposition, samples are exposed to rather high temperatures. However, the recommended maximal temperature for patterned CSAR resist is 130  $^{\circ}\text{C}$  [63], which significantly limits the process temperature of ALD. Two ALD processes that deposit  $\text{TiO}_2$  under relatively low temperatures are

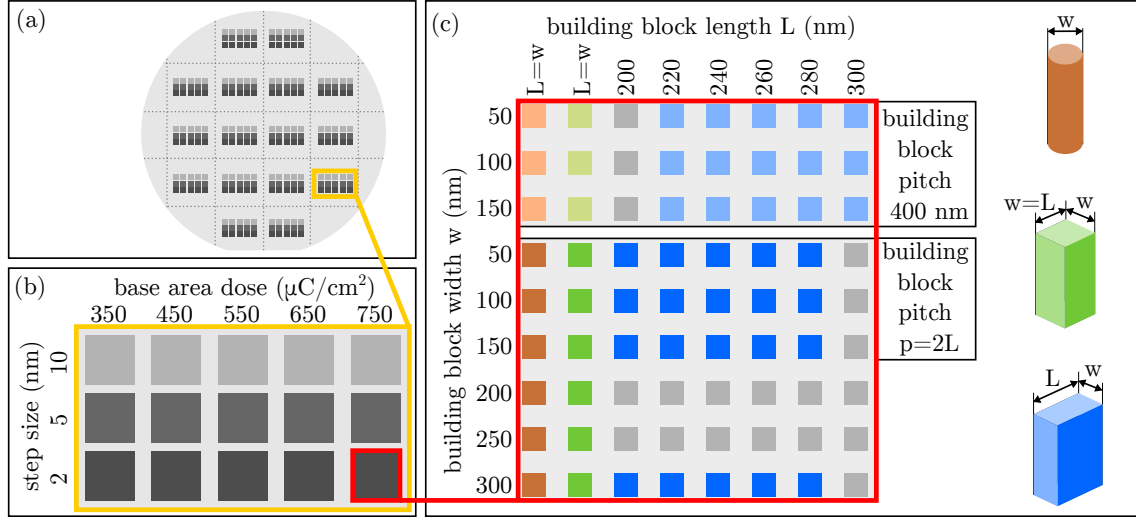


**Figure 18:** Design of the structures patterned at the Institute of Scientific Instruments CAS. (a) Wafer design comprising individual chips described in panels b,c. (b) Area dose and step size variations in each of the patterned chips. (c) Design of the building block arrays. S. Krátký is gratefully acknowledged for his involvement in the involvement in the development of panels a,b and the preparation of the resist mould.



**Table 4.2:** Overview of the atomic layer deposition rates of  $\text{TiO}_2$  (precursor: tetrakis(dimethylamido)titanium,  $(\text{Ti}(\text{NMe}_2))_4$ ) ALD processes with relatively low process temperature.

material	process type	temperature ( $^{\circ}\text{C}$ )	rate ( $\text{\AA}/\text{cycle}$ )	cycle duration	duration for 150 nm
$\text{TiO}_2$	thermal	100	ca. 0.52	2 min	96 hours
$\text{TiO}_2$	plasma	100	ca. 0.59	1.5 min	63.5 hours

listed in Tab. 4.2. Out of these, the plasma process seems to be more advantageous due to its significantly shorter duration compared to the thermal process of the same temperature. However, the oxygen plasma used in the plasma process might deteriorate the pre-patterned resist mold and thus, the resulting structures might be deformed. Hence, the thermal ALD process was chosen for the deposition of the titanium dioxide layer into the prepared resist mold.

To make sure that the selected process does not harm the resist mould, a shorter 19-hour deposition was carried out first, with an ALD system Fiji 200 (Ultratech/CambridgeNanoTech). The quality of the deposited layer was probed with photoelectron spectroscopy. With an approach to data interpretation identical to the experiment shown in Fig. 14, it has been confirmed that the stoichiometry of the  $\text{TiO}_2$  layer prepared by ALD is  $\text{Ti}_1\text{O}_{1.96}$ . This is a satisfying result and in com-

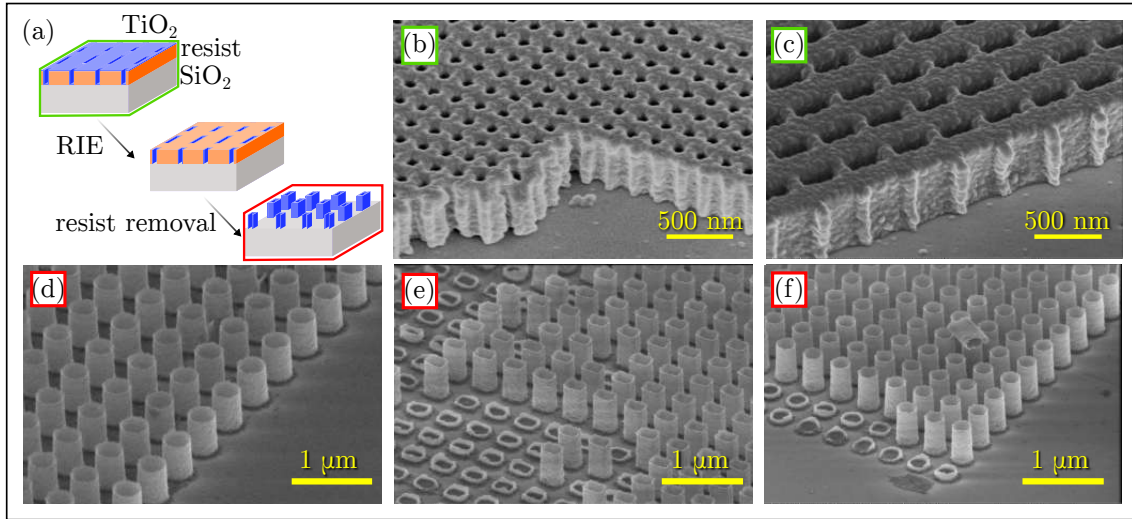


**Figure 19:** Primary testing of atomic layer deposition and reactive ion etching. (a) Schematic of the fabrication steps presented in this figure. (b),(c) SEM images of the resist mould covered by ca. 30 nm of  $\text{TiO}_2$ , taken before the reactive ion etching. (d)-(f) SEM images of hollow  $\text{TiO}_2$  structures. Due to their fragile construction, many structures are damaged. All of the presented micrographs were taken under  $50^{\circ}$  tilt of the sample towards the electron beam.

parison to the titanium dioxide layer prepared by magnetron sputtering, it shows a better stoichiometry of the deposited layer. Subsequently, the test sample was observed with SEM Verios 460L. The resist mold seemed to maintain its designed shape, as illustrated in micrographs in Fig. 19b,c. To reveal the underlying resist mould, RIE of the upper 30 nm thin  $\text{TiO}_2$  layer was performed across the sample surface. The etching was performed in the same way as described previously, for 105 s with oxygen flow of 1 sccm. After RIE, the test sample was submerged in dioxolane for 30 minutes to dissolve the now-revealed resist mould. Afterwards, the test sample was immersed in isopropyl alcohol and then dried with a nitrogen gun. After the removal of all unwanted residuals, the created structures were observed with SEM Verios 460L. As shown in Figs. 19d-f, the resulting structures turned out to be hollow pipe-like pillars of rectangular and circular profiles. These structures also seem to have more defined shapes than those prepared by the strategy presented in section 4.1 which uses magnetron sputtering for the  $\text{TiO}_2$  deposition. The atomic layer deposition of  $\text{TiO}_2$  ensured the minimal size of  $\text{TiO}_2$  grains in the structures, which improves their overall shape. However, as presented in Figs. 19d-f, the currently fabricated structures are slightly damaged – some of the pillars broke from the substrate due to their fragile, thin-wall construction. Once the deposition of a thicker layer is conducted, more stability should be granted for structures fabricated by this strategy. To sum up, the shown ALD-based fabrication strategy will most likely surpass the RIE-based fabrication strategy from section 4.1 once the resist mold will be completely filled by ALD with a  $\text{TiO}_2$  layer of sufficient thickness in the future.

## 4.2 Optical characterization of the metasurfaces

The optical responses of the fabricated metasurfaces were characterized with a coherence-controlled holographic microscope developed at BUT. The relative phase shift and relative field transmissivity measurements of the individual building block arrays were measured twice to compare the performance of the metasurfaces under unpolarized irradiation of two different wavelengths: 550 nm and 650 nm light sources were used. For the purposes of this thesis, the relative phase shift (RPS) denotes:

$$\text{RPS} = \text{phase shift (substrate with structures)} - \text{phase shift (sole substrate)} \quad (7)$$

and the relative field transmissivity (RFT) is defined as:

$$\text{RFT} = \frac{\text{field transmissivity (substrate with structures)}}{\text{field transmissivity (sole substrate)}}. \quad (8)$$

These two characteristics were measured for metasurfaces consisting of square or circular building blocks (for the particular design of these structures, see Fig. 15 and Fig. 17).

Figs. 20a,c show that for both of the tested illumination wavelengths, the available RPS of the fabricated metasurface building blocks exceeds  $2\pi$ . The stagnation of the plots presented in these figures for the smallest fabricated structures (characteristic dimension 50 nm and 75 nm) is caused by fabrication imperfections, namely the lack of these structures in the measured fields. Similarly, the structures with larger characteristic dimensions happened to melt together instead of forming big building blocks with narrow space in between each other. Hence, for the further fabrication of metasurfaces, structures with characteristic dimension from interval (75–300) nm will be used. Furthermore, it should be noted that in both of these graphs, the square building blocks shift the phase a little more than the circular ones. This phenomenon is a natural consequence of squares with side  $a$  occupying a

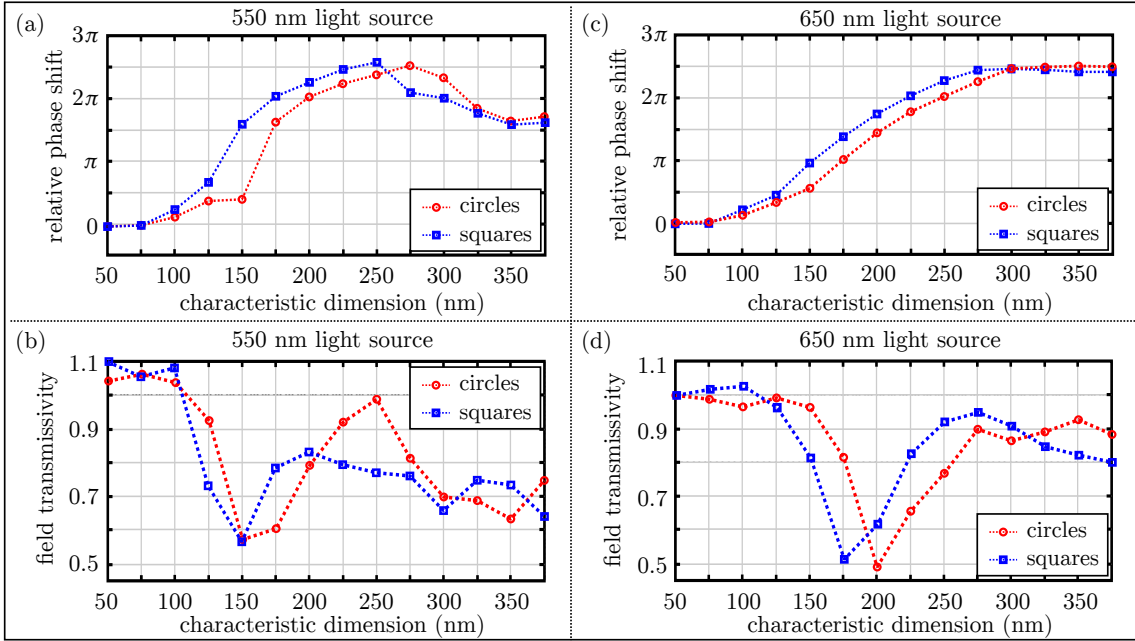


**Figure 20:** CCHM measurements of  $\text{TiO}_2$  building block arrays with square (blue) and circular (red) design. (a),(c) Relative phase shift measured with a light source of wavelength (a) 550 nm, (c) 650 nm. For both illuminations, the phase shift range of  $2\pi$  was covered. (b),(d) Relative field transmissivity measured with light source of wavelength (b) 550 nm, (d) 650 nm. For structures with phase shift around  $\pi$ , the relative field transmissivity drops significantly. We do believe that these measurements are strongly affected by the interference of the measured structures with the interference used to reconstruct a hologram in CCHM measurements and hence, Fig. 21 presents more accurate results. For further specification of the presented entities, see equations (7),(8).

bigger area than circles with diameter  $a$  – the effective refractive index of the metasurfaces composed of square building blocks is thus bigger than that of the circular ones. Hence, the measured phase shifts are in agreement with those presented by equation (3) in section 2.2.

The variation of the amplitude of the metasurface-affected light was first determined by the analysis of the conducted CCHM measurement in a way already described in Fig. 6. The yielded outcomes are graphically depicted in Fig. 20b,d as RFT values. An inconsistency of the relative field transmission was observed: in both illumination cases for both building block types, a sudden drop of the relative field transmissivity appeared for building blocks with a phase shift around  $\pi$ . This is most likely caused by the unfortunate combination of the interference pattern originating in the CCHM hologram reconstruction with the interference pattern generated by the light, which partially did and partially did not couple with the metasurface building blocks. To evaluate the relative field transmissivity of individual building block arrays without these unwanted artifacts, yet another measurement was performed with conventional optical spectroscopy.

For optical spectroscopy measurements of the fabricated structures, an experiment was carried out in a transmission geometry with unpolarized white light source. The adjustable slit of the spectrometer was opened to 800  $\mu\text{m}$  and a diffraction grating with 1200 grooves per mm was used. First, a background spectrum was recorded with shuttered illumination. All of the following measurements were corrected by subtraction of this background signal. For each measurement point, a reference signal was measured in a nearby point with no metasurface structures. Subsequently, the signal detected from the measurement point was divided by the signal obtained from the reference, as already indicated in Fig. 7. In the performed experiment, fields of circle-, square- and wall-like pillars with different characteristic dimensions were measured, as illustrated in Fig. 21a. The results of these measurements are presented in Figs. 21b-d. For linear structures, a slight shift of the transmittance dip towards larger wavelengths can be observed with increasing characteristic dimension (pink, purple, dark blue in Fig. 21b). Circular metasurface building blocks show similar behavior, especially for characteristic dimensions of (100–200) nm (dark-blue, blue, aqua, green in Fig. 21c). In this figure, the relative intensities of the transmitted light are compared to those measured via CCHM (diamond symbols of respective colors). Clearly, the results obtained by these two methods do not show the same results. To fully resolve the meaning and significance of the yielded data (especially the resonances which cause the measured spectra to be wavy), a comparison with numerical simulations is planned. Eventually, based on the results of these simulations, the reliability of these measurement methods may be established, too. Similar to the results obtained from the measurements of circular nanopillars, the outcomes of

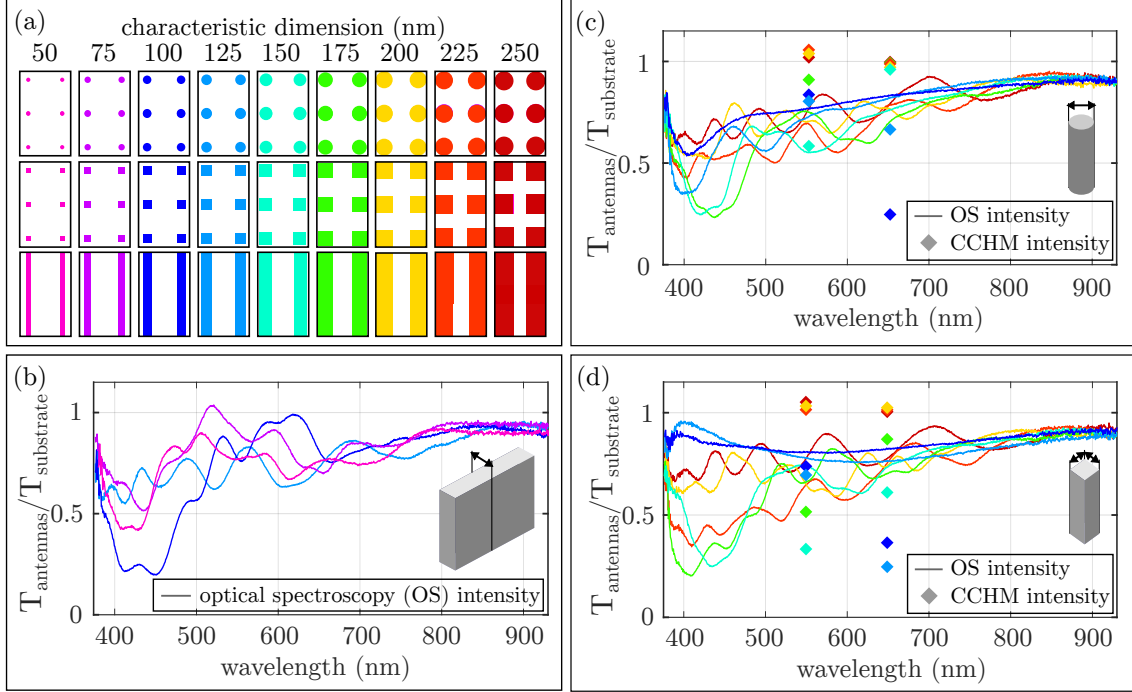


**Figure 21:** Optical spectroscopy of fabricated structures. (a) Overview of the measured structures and their geometries, color legend for panels (b)-(d). (b) Optical spectroscopy of variously wide lines. (c) Comparison of optical responses of circular and (d) square-like metasurface building blocks measured with optical spectroscopy (lines) and CCHM (diamonds). For both circles and squares, the measured relative transmissivity values do not overlap. To confirm the reliability of these measurements, numerical simulations will be employed in the future.

the CCHM and optical spectroscopy differ for square-like pillars, too (see Fig. 21d). Additionally, the previously observed trend of the transmittance dip redshift with the growing characteristic dimension of the building blocks is not observable in these structures. This might be caused by the faulty fabrication of fields with building blocks of characteristic dimensions (100–125) nm. However, if these fields were truly incorrect, inconsistencies would appear in relative phase shifts exhibited by these arrays too. As this is not the case, the planned numerical simulations are believed to clarify the origin of these differences.

To probe the functionality of the fabricated half-wave plate metasurfaces (such as those in Fig. 17b,c), several measurements of the RFT (defined by relation (8)) were conducted. The fabricated half-wave plates were placed between two crossed polarizers and upon variations of the angle  $\alpha$  held between the analyzer and half-wave plate, the transmissivity of this system was measured. Fig. 22a shows a schematic of the performed experiments: the half-wave plate structures were measured at two wavelengths (550 nm, 650 nm) with fixed positions of both polarizer and analyzer,

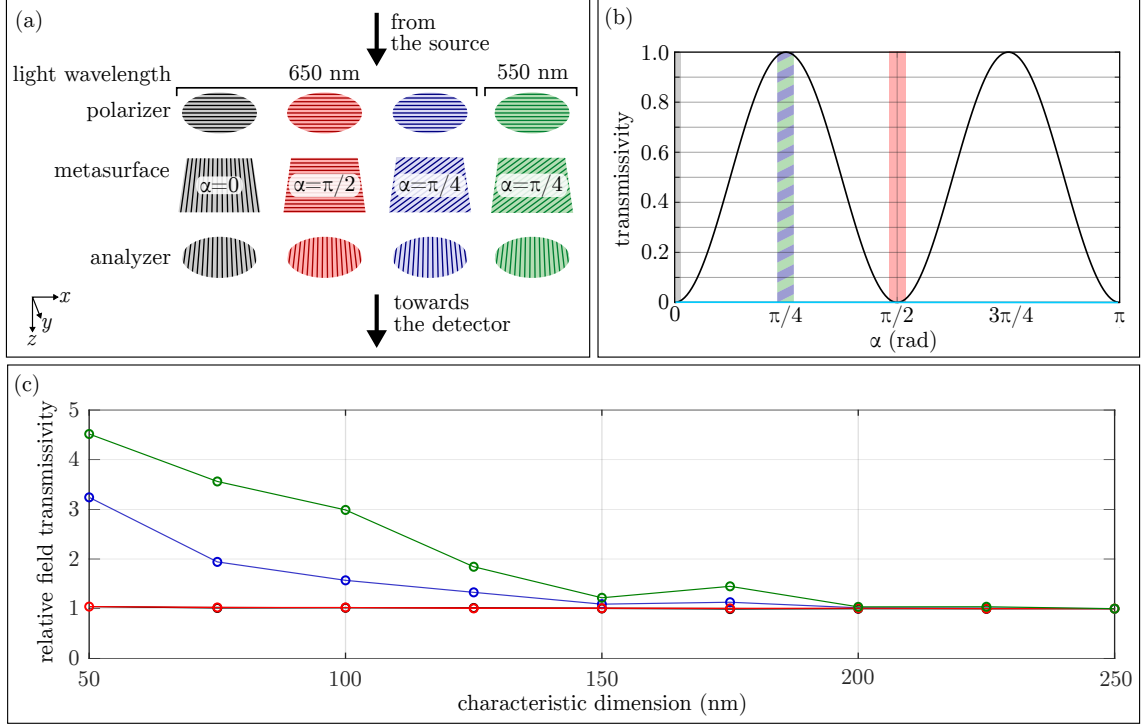


**Figure 22:** Probing of the functionality of fabricated metasurface half-wave plates. (a) Schematic of the performed measurements. For fixed polarizer and analyzer positions, relative field transmissivity was measured for three different rotations of the metasurface building blocks and two wavelengths. (b) Dependence of the system transmissivity on the rotation ( $\alpha$ ) of the metasurface fast axis towards the transmission axis of the analyzer (black line). The cyan line shows the transmissivity of the system if no half-wave plate is present. (c) Relative field transmissivity of wall-like metasurfaces with various characteristic dimension of the walls measured for four configurations shown in panel (a). The reference was measured on a clear fused silica substrate.

in three different rotations with respect the analyzer,  $\alpha = (0, \pi/4, \pi/2)$ .

In the theory of matrix optics, the light which propagated through the optical system used for this measurement can be described with Jones' matrices as follows:

$$\begin{pmatrix} E_x \\ E_y \end{pmatrix} = \begin{pmatrix} \cos^2 \varphi & \cos \varphi \sin \varphi \\ \cos \varphi \sin \varphi & \sin^2 \varphi \end{pmatrix} \begin{pmatrix} \cos \alpha & -\sin \alpha \\ \sin \alpha & \cos \alpha \end{pmatrix} \begin{pmatrix} 1 & 0 \\ 0 & e^{-i\delta} \end{pmatrix} \begin{pmatrix} \cos \alpha & \sin \alpha \\ -\sin \alpha & \cos \alpha \end{pmatrix} \begin{pmatrix} \cos \vartheta \\ \sin \vartheta \end{pmatrix}. \quad (9)$$

In the respective order, the matrices on the right side of this equation represent: polarizer (analyzer) rotated by the angle  $\varphi$  with respect to the  $x$  axis, coordinate system rotation by  $\alpha$ , which is the angle between the fast axis of the half-wave plate (parallel with the fabricated wall-like structures) and the  $x$  axis, wave plate retarder, coordinate system rotation by  $-\alpha$ , and the incident light of linear polarization rotated by  $\vartheta$  from the  $x$  axis. If the variables are substituted with values corresponding

to the orientations of the polarizer ( $\vartheta = 0$ ) and the analyzer ( $\varphi = \pi/2$ ) used in the performed experiment for the case of a half-wave plate ( $\delta = \pi$ ), the transmissivity  $T$  of the system can be expressed as:

$$T = E_x^2 + E_y^2 = 0 + (2\sin\alpha\cos\alpha)^2 = \sin^2\left(\frac{\alpha}{2}\right). \quad (10)$$

This relation is also plotted in Fig. 22b with a black line. As visible in the presented plot, the maximum of the transmitted light can be achieved for  $\alpha = \pi/4$ , while for  $\alpha = 0$  and  $\alpha = \pi/2$ , the system should transmit as much light as it would without the half-wave plate (marked with cyan line in Fig. 22b) – which, in the case of crossed polarizers, should be a near-zero value. The experimental results show that for  $\alpha = 0$  and  $\alpha = \pi/2$ , the transmissivity of the half-wave plate metasurface fields is very similar to that exhibited by a clear substrate, i.e., that the relative field transmissivity is close to one (see Fig. 22c). Simultaneously, for wave plates rotated by  $\pi/4$  with respect to the analyzer transmission axis, the transmissivity of the metasurface fields is higher than that of the clear substrate, as denoted by values greater than one in the plot in Fig. 22c. Even though the observed results seem to confirm the half-wave plate nature of the fabricated metasurfaces, a more detailed experiment would be suitable for precise characterization of the created half-wave plates. Namely, if the measurements would be carried out in more than three variations of  $\alpha$ , one angle could be estimated which would correspond to the maximal value of relative field transmission. Then, the conversion efficiency of the half-wave plate could be estimated if all of the measured RFT values would be normalized to this found maximum. In summary, four of the fabricated metasurfaces show enhanced transmission in comparison to the used substrate. Seemingly, the most effective half-wave plate metasurfaces are those composed of (50–75) nm wide wall-like structures.





## 5 CONCLUSIONS

The aim of this work was to design, fabricate, and characterize an optical metasurface serving as a modern optical component. After a short introduction into the thesis, the second chapter defined the term metasurfaces and then presented some of the most common applications and working principles of metasurfaces. Further, attention was brought to two specific applications of metasurfaces in optics: half-wave plate and diffractive beam splitter, as these were later also fabricated and characterized. The chapter was closed by the description of methods used for optical characterization of metasurfaces in this thesis, namely coherence-controlled holographic microscopy (CCHM) and optical spectroscopy.

The third chapter provided a theoretical description of the working principles of methods used in sample fabrication. Several thin film deposition techniques were addressed. Then, the choice of electron beam lithography as the fabrication technique of optical metasurfaces was explained, and its detailed description was presented. Etching strategies for selected commonly used materials were mentioned, along with an introduction to wet etching and reactive ion etching.

Finally, the fourth chapter was dedicated to the presentation of the experimental work and its results. In the early stages of this work, two fabrication strategies (see Fig. 13) were considered for the fabrication of high aspect ratio dielectric structures, which could serve as building blocks for optical metasurfaces. Eventually, only one of them was carried out entirely, as it was feasible independently by the author in the laboratories of CEITEC Nano RI. This fabrication strategy employs selective reactive ion etching of a dielectric layer through a metallic hardmask prepared by electron beam lithography. The resulting metasurfaces prepared by this fabrication strategy were later optically characterized. The other proposed strategy was dependent on the collaboration with the Institute of Scientific Instruments of the Czech Academy of Sciences, as it required electron beam patterning of a thick resist layer, feasible only with a lithographic tool operating with high-energy electrons. As of now, this strategy has resulted solely in the fabrication of high aspect ratio  $\text{TiO}_2$  nanopillars in a hollow, pipe-like modification. To prepare the proposed structures filled with  $\text{TiO}_2$ , a 96-hour long ALD deposition needs to be conducted. In summary, the work on both of these fabrication strategies has provided a number of useful outcomes for the future fabrication of metasurfaces at BUT: The complete high aspect ratio metasurface fabrication strategy based on RIE is considered to be one of the main outcomes of this work. The deposition process of  $\text{TiO}_2$  by magnetron sputtering was optimized, even though further optimization might be needed for the process to be stable for the long times needed for thick layer depositions. Interestingly, it has been found that to enhance the adhesion between

the electron beam resist and  $\text{TiO}_2$  surface, only the AR300-80 adhesion promoter worked. Then, using a chromium hardmask, reactive ion etching of  $\text{TiO}_2$  was performed with varying supply of oxygen in the etching gas mixture (30 sccm  $\text{CHF}_3$ , (1-5) sccm  $\text{O}_2$ , 50 sccm Ar). Results achieved in this experiment are in agreement with a similar study in [66]. Different dosage of oxygen in the etching gas mixture causes variations in the etching rate, selectivity of the chromium mask, and sidewall profiles of the fabricated structures. Wall-like structures for half-wave plates were fabricated in various sizes along with sets of circular and square-profiled structures for a future metasurface diffractive beam splitter. Furthermore, this thesis analyzed the performance and optical response of the fabricated structures. First, the phase quantification measurement conducted with CCHM has proven that the fabricated nanopillars with circular and square-like profiles are able to shift the phase of transmitted light by more than  $2\pi$  for light of wavelengths 550 nm and 650 nm. Hence, these structures can be incorporated into the design of a diffractive beam splitter in the future. Further, CCHM was also used to determine the transmissivity of the fabricated structures. The results of the CCHM transmissivity measurements were compared with spectra yielded from optical spectroscopy measurements. As the obtained results did not match, numerical simulations will be used in the future to establish the relevance of the performed measurements and resolve the significance of the yielded outcomes. Finally, the performance of the fabricated half-wave plate metasurfaces was analyzed by conducting a series of measurements with a different rotation of the metasurface's fast axis with respect to a couple of crossed polarizers. Four of the fabricated metasurface arrays show the desired half-wave plate behavior, while the most effective metasurfaces seem to be those composed of (50-75) nm wide wall-like building blocks.

In summary, this thesis demonstrated a successful fabrication and optical characterization of metasurface half-wave plates and building blocks for diffractive beam splitters in the visible range of the electromagnetic spectrum.

# REFERENCES

- [1] Yu, N., Genevet, P., Kats, M. A., *et al.* Light propagation with phase discontinuities: generalized laws of reflection and refraction. *Science*, 334 (6054), **2011**, pp. 333–337. doi:[10.1126/science.1210713](https://doi.org/10.1126/science.1210713).
- [2] Zhang, L., Mei, S., Huang, K., and Qiu, C.-W. Advances in full control of electromagnetic waves with metasurfaces. *Advanced Optical Materials*, 4 (6), **2016**, pp. 818–833. doi:[10.1002/adom.201500690](https://doi.org/10.1002/adom.201500690).
- [3] Yu, N. and Capasso, F. Flat optics with designer metasurfaces. *Nature Materials*, 13, **2016**, pp. 139–150. doi:[10.1038/nmat3839](https://doi.org/10.1038/nmat3839).
- [4] Glybovski, S. B., Tretyakov, S. A., Belov, P. A., *et al.* Metasurfaces: from microwaves to visible. *Physics Reports*, 634, **2016**, pp. 1–72. doi:[10.1016/j.physrep.2016.04.004](https://doi.org/10.1016/j.physrep.2016.04.004).
- [5] Bukhari, S. S., Vardaxoglou, J. Y., and Whittow, W. Metasurfaces review: definitions and applications. *Applied Sciences*, 9 (13), **2019**, p. 2727. doi:[10.3390/app9132727](https://doi.org/10.3390/app9132727).
- [6] Liu, Y. and Zhang, X. *Metamaterial*. Available at <https://www.britannica.com/topic/metamaterial> (Accessed 26 June 2020).
- [7] Li, A., Forati, E., and Sievenpiper, D. Study of the electric field enhancement in resonant metasurfaces. *Journal of Optics*, 19 (12), **2017**, p. 125104. doi:[10.1088/2040-8986/aa97ea](https://doi.org/10.1088/2040-8986/aa97ea).
- [8] Decker, M., Staude, I., Falkner, M., *et al.* High-efficiency dielectric Huygens’ surfaces. *Advanced Optical Materials*, 3 (6), **2015**, pp. 813–820. doi:[10.1002/adom.201400584](https://doi.org/10.1002/adom.201400584).
- [9] Kamali, S. M., Arbabi, E., Arbabi, A., and Faraon, A. A review of dielectric optical metasurfaces for wavefront control. *Nanophotonics*, 7 (6), **2018**, pp. 1041–1068. doi:<https://doi.org/10.1515/nanoph-2017-0129>.
- [10] Xu, H.-X., Hu, G., Han, L., *et al.* Chirality-assisted high-efficiency metasurfaces with independent control of phase, amplitude, and polarization. *Advanced Optical Materials*, 7 (4), **2019**, p. 1801479. doi:[10.1002/adom.201801479](https://doi.org/10.1002/adom.201801479).
- [11] Park, J., Kang, J.-H., Kim, S. J., *et al.* Dynamic reflection phase and polarization control in metasurfaces. *Nano Letters*, 17 (1), **2017**, pp. 407–413. doi:[10.1021/acs.nanolett.6b04378](https://doi.org/10.1021/acs.nanolett.6b04378).
- [12] Lalanne, P. and Chavel, P. Metalenses at visible wavelengths: past, present, perspectives. *Laser & Photonics Reviews*, 11 (3), **2017**, p. 1600295. doi:[10.1002/lpor.201600295](https://doi.org/10.1002/lpor.201600295).
- [13] Feynman, R. P., Leighton, R. B., and Sands, M. *The Feynman lectures on physics: mainly mechanics, radiation, and heat*. Basic Books, 50th New Millenium ed., **2011**. ISBN 978-0-465-02493-3.
- [14] Khorasaninejad, M. and Capasso, F. Metalenses: versatile multifunctional photonic components. *Science*, 358 (6367), **2017**. doi:[10.1126/science.aam8100](https://doi.org/10.1126/science.aam8100).
- [15] Mueller, J. P. B., Rubin, N. A., Devlin, R. C., *et al.* Metasurface polarization optics: independent phase control of arbitrary orthogonal states of polarization. *Physical Review Letters*, 118, **2017**, p. 113901. doi:[10.1103/PhysRevLett.118.113901](https://doi.org/10.1103/PhysRevLett.118.113901).
- [16] Avayu, O., Almeida, E., Prior, Y., and Ellenbogen, T. Composite functional metasurfaces for multispectral achromatic optics. *Nature Communications*, 8, **2017**, p. 14992. doi:[10.1021/ncomms14992](https://doi.org/10.1021/ncomms14992).

- [17] Chen, W. T., Zhu, A. Y., Sisler, J., *et al.* Broadband achromatic metasurface-refractive optics. *Nano Letters*, 18 (12), **2018**, pp. 7801–7808. doi:[10.1021/acs.nanolett.8b03567](https://doi.org/10.1021/acs.nanolett.8b03567).
- [18] Xiong, X., Jiang, S.-C., Hu, Y.-H., *et al.* Structured metal film as a perfect absorber. *Advanced Materials*, 25 (29), **2013**, pp. 3994–4000. doi:[10.1002/adma.201300223](https://doi.org/10.1002/adma.201300223).
- [19] Lin, J., Genevet, P., Kats, M. A., *et al.* Nanostructured holograms for broadband manipulation of vector beams. *Nano Letters*, 13 (9), **2013**, pp. 4269–4274. doi:[10.1021/nl402039y](https://doi.org/10.1021/nl402039y).
- [20] Arbabi, A., Briggs, R. M., Horie, Y., *et al.* Efficient dielectric metasurface collimating lenses for mid-infrared quantum cascade lasers. *Optics Express*, 23 (26), **2015**, pp. 33310–33317. doi:[10.1364/OE.23.033310](https://doi.org/10.1364/OE.23.033310).
- [21] Yu, Y. F., Zhu, A. Y., Paniagua-Domínguez, R., *et al.* High-transmission dielectric metasurface with  $2\pi$  phase control at visible wavelengths. *Laser & Photonics Reviews*, 9 (4), **2015**, pp. 412–418. doi:[10.1002/lpor.201500041](https://doi.org/10.1002/lpor.201500041).
- [22] Huang, Y.-W., Chen, W. T., Tsai, W.-Y., *et al.* Aluminum Plasmonic Multicolor Meta-Hologram. *Nano Letters*, 15 (5), **2015**, pp. 3122–3127. doi:[10.1021/acs.nanolett.5b00184](https://doi.org/10.1021/acs.nanolett.5b00184).
- [23] Shi, Z., Khorasaninejad, M., Huang, Y.-W., *et al.* Single-Layer Metasurface with Controllable Multiwavelength Functions. *Nano Letters*, 18 (4), **2018**, pp. 2420–2427. doi:[10.1021/acs.nanolett.7b05458](https://doi.org/10.1021/acs.nanolett.7b05458).
- [24] Khorasaninejad, M., Shi, Z., Zhu, A. Y., *et al.* Achromatic metalens over 60 nm bandwidth in the visible and metalens with reverse chromatic dispersion. *Nano Letters*, 17 (3), **2017**, pp. 1819–1824. doi:[10.1021/acs.nanolett.6b05137](https://doi.org/10.1021/acs.nanolett.6b05137).
- [25] Lin, D., Fan, P., Hasman, E., and Brongersma, M. L. Dielectric gradient metasurface optical elements. *Science*, 345 (6194), **2014**, pp. 298–302. doi:[10.1126/science.1253213](https://doi.org/10.1126/science.1253213).
- [26] Zheng, G., Mühlenbernd, H., Kenney, M., *et al.* Metasurface holograms reaching 80% efficiency. *Nature Nanotechnology*, 10, **2015**, pp. 308–312. doi:[10.1038/nnano.2015.2](https://doi.org/10.1038/nnano.2015.2).
- [27] Fan, Q., Huo, P., Wang, D., *et al.* Visible light focusing flat lenses based on hybrid dielectric-metal metasurface reflector-arrays. *Scientific Reports*, 7 (45044), **2017**. doi:[10.1038/srep45044](https://doi.org/10.1038/srep45044).
- [28] Meinzer, N., Barnes, W. L., and Hooper, I. R. Plasmonic meta-atoms and metasurfaces. *Nature Photonics*, 8, **2014**, pp. 889–898. doi:[10.1038/nphoton.2014.247](https://doi.org/10.1038/nphoton.2014.247).
- [29] Dong, Y., Xu, Z., Li, N., *et al.* Si metasurface half-wave plates demonstrated on a 12-inch CMOS platform. *Nanophotonics*, 9 (1), **2019**, pp. 149–157. doi:[10.1515/nanoph-2019-0364](https://doi.org/10.1515/nanoph-2019-0364).
- [30] Kabiri, A., Girgis, E., and Capasso, F. Metasurface-based half-wave plate. In *2013 IEEE Antennas and Propagation Society International Symposium (APSURSI)*, pp. 322–323. 2013. doi:[10.1109/APS.2013.6710822](https://doi.org/10.1109/APS.2013.6710822).
- [31] Ding, F., Wang, Z., He, S., *et al.* Broadband high-efficiency half-wave plate: A supercell-based plasmonic metasurface approach. *ACS Nano*, 9 (4), **2015**, pp. 4111–4119. doi:[10.1021/acs.nano.5b00218](https://doi.org/10.1021/acs.nano.5b00218).
- [32] Li, J., Zhang, Y., Jin, R., *et al.* Excitation of plasmon toroidal mode at optical frequencies by angle-resolved reflection. *Optics Letters*, 39 (23), **2014**, pp. 6683–6686. doi:[10.1364/OL.39.006683](https://doi.org/10.1364/OL.39.006683).

- [33] Zhou, X.-T., Jin, R.-C., Wang, J., *et al.* All-metal metasurface polarization converter in visible region with an in-band function. *Applied Physics Express*, 12 (9), **2019**, p. 092010. doi:[10.7567/1882-0786/ab3c0c](https://doi.org/10.7567/1882-0786/ab3c0c).
- [34] Salter, P. and Booth, M. Adaptive optics in laser proceedings. *Light: Science & Applications*, 8 (110), **2019**. doi:[10.1038/s41377-019-0215-1](https://doi.org/10.1038/s41377-019-0215-1).
- [35] Li, J., Liu, C., Wu, T., *et al.* Efficient polarization beam splitter based on all-dielectric metasurface in visible region. *Nano Express*, 14 (34), **2019**, pp. 911–914. doi:[10.1186/s11671-019-2867-4](https://doi.org/10.1186/s11671-019-2867-4).
- [36] Lin, Y., Wang<sup>1</sup>, M., Sui<sup>1</sup>, Z., *et al.* Highly efficient beam splitter based on all-dielectric metasurfaces. *Japanese Journal of Applied Physics*, 58, **2019**, p. 060918. doi:[10.7567/1347-4065/ab219b](https://doi.org/10.7567/1347-4065/ab219b).
- [37] Kolman, P. and Chmelík, R. Coherence-controlled holographic microscope. *Opt. Express*, 18 (21), **2010**, pp. 21990–22004. doi:[10.1364/OE.18.021990](https://doi.org/10.1364/OE.18.021990).
- [38] Slabý, T. *New generation of coherence-controlled holographic microscope*. Ph.D. thesis, Brno University of Technology, **2014**.
- [39] Kreis, T. Digital holographic interference-phase measurement using the Fourier-transform method. *Journal of the Optical Society of America A*, 3 (6), **1986**, pp. 847–855. doi:[10.1364/JOSAA.3.000847](https://doi.org/10.1364/JOSAA.3.000847).
- [40] Rice, A., Allerman, A., Crawford, M., *et al.* Effects of deposition temperature and ammonia flow on metal-organic chemical vapor deposition of hexagonal boron nitride. *Journal of Crystal Growth*, 485, **2018**, pp. 90–95. doi:[10.1016/j.jcrysgro.2017.12.011](https://doi.org/10.1016/j.jcrysgro.2017.12.011).
- [41] Zhao, P., Kumamoto, A., Kim, S., *et al.* Self-limiting chemical vapor deposition growth of monolayer graphene from ethanol. *The Journal of Physical Chemistry C*, 117 (20), **2013**, pp. 10755–10763. doi:[10.1021/jp400996s](https://doi.org/10.1021/jp400996s).
- [42] Nam, S.-W., Lee, M.-H., Lee, S.-H., *et al.* Sub-10-nm nanochannels by self-sealing and self-limiting atomic layer deposition. *Nano Letters*, 10 (9), **2010**, pp. 3324–3329. doi:[10.1021/nl100999e](https://doi.org/10.1021/nl100999e).
- [43] Ritala, M. and Leskelä, M. Atomic layer deposition. In H. S. Nalwa (ed.), *Handbook of Thin Films*, pp. 103 – 159. Academic Press, **2002**. ISBN 978-0-12-512908-4.
- [44] Johnson, R. W., Hultqvist, A., and Bent, S. F. A brief review of atomic layer deposition: from fundamentals to applications. *Materials Today*, 17 (5), **2014**, pp. 236 – 246. doi:[10.1016/j.mattod.2014.04.026](https://doi.org/10.1016/j.mattod.2014.04.026).
- [45] Gudmundsson, J. T. and Lundin, D. Introduction to magnetron sputtering. In D. Lundin, T. Minea, and J. T. Gudmundsson (eds.), *High power impulse magnetron sputtering*, pp. 1–48. Elsevier, 2020. ISBN 978-0-128-12454-3.
- [46] AJA International, Inc. *What is sputtering?*. Available at <http://www.ajaint.com/what-is-sputtering.html> (Accessed 26 June 2020).
- [47] Harsha, K. *Principles of physical vapor deposition of thin films*. Elsevier, **2005**. ISBN 978-0-080-48031-2.
- [48] Lu, C. and Czanderna, A. *Applications of piezoelectric quartz crystal microbalances*. Elsevier Science Publishers, **1984**. ISBN 0-444-42277-3.

- [49] Yue, W., Gao, S., Lee, S.-S., *et al.* Highly reflective subtractive color filters capitalizing on a silicon metasurface integrated with nanostructured aluminum mirrors. *Laser & Photonics Reviews*, 11 (3), **2017**, p. 1600285. doi:[10.1002/lpor.201600285](https://doi.org/10.1002/lpor.201600285).
- [50] Rollo, S., Rani, D., Olthuis, W., and García, C. P. Single step fabrication of silicon resistors on SOI substrate used as thermistors. *Scientific Reports*, 9, **2019**, p. 2835. doi:[10.1038/s41598-019-38753-x](https://doi.org/10.1038/s41598-019-38753-x).
- [51] van Dorp, W. F. Theory: electron-induced chemistry. In A. Robinson and R. Lawson (eds.), *High power impulse magnetron sputtering*, pp. 115–176. Elsevier, 2016. ISBN 978-0-081-00354-1.
- [52] Okoroanyanwu, U. *Chemistry and lithography*. SPIE, **2010**. ISBN 978-0-8194-7562-6.
- [53] Murali, R. Metrology for grayscale lithography. *AIP Conference Proceedings*, 931 (1), **2007**, pp. 419–422. doi:[10.1063/1.2799410](https://doi.org/10.1063/1.2799410).
- [54] Mortelmans, T., Kazazis, D., Guzenko, V. A., *et al.* Grayscale e-beam lithography: Effects of a delayed development for well-controlled 3D patterning. *Microelectronic Engineering*, 225, **2020**, p. 111272. doi:<https://doi.org/10.1016/j.mee.2020.111272>.
- [55] Orloff, J. *Handbook of charged particle optics, second edition*. CRC Press, **2009**. ISBN 978-0-471-44339-1.
- [56] Liljeborg, A. *Raith 150 e-beam lithography software*. Available at <http://nanophys.kth.se/nanophys/facilities/nfl/manual/index.html> (Accessed 26 June 2020).
- [57] Šamořil, T. *Aplikace fokusovaného iontového a elektronového svazku v nanotechnologiích*. Ph.D. thesis, Brno University of Technology, **2015**.
- [58] Reinhardt, K. A. and Reidy, R. F. *Handbook of cleaning for semiconductor manufacturing*. Wiley, **2011**. ISBN 978-0-470-62595-8.
- [59] Coburn, J. W. and Winters, H. F. Ion- and electron-assisted gas-surface chemistry – An important effect in plasma etching. *Journal of Applied Physics*, 50 (5), **1979**, pp. 3189–3196. doi:[10.1063/1.326355](https://doi.org/10.1063/1.326355).
- [60] Gouttebaron, R., Cornelissen, D., Snyders, R., *et al.* XPS study of TiO<sub>x</sub> thin films prepared by d.c. magnetron sputtering in Ar–O<sub>2</sub> gas mixtures. *Surface and Interface Analysis*, 30 (1), **2000**, pp. 527–530. doi:[10.1002/1096-9918\(200008\)30:1<527::AID-SIA834>3.0.CO;2-Z](https://doi.org/10.1002/1096-9918(200008)30:1<527::AID-SIA834>3.0.CO;2-Z).
- [61] Babelon, P., Dequiedt, A., Mostéfa-Sba, H., *et al.* SEM and XPS studies of titanium dioxide thin films grown by MOCVD. *Thin Solid Films*, 322 (1), **1998**, pp. 63–67. doi:[https://doi.org/10.1016/S0040-6090\(97\)00958-9](https://doi.org/10.1016/S0040-6090(97)00958-9).
- [62] Allresist. *Adhesion promoter for AR resists*. Available at [https://www.allresist.com/wp-content/uploads/sites/2/2018/01/allresist\\_produkinfos\\_ar300-80\\_english.pdf](https://www.allresist.com/wp-content/uploads/sites/2/2018/01/allresist_produkinfos_ar300-80_english.pdf) (Accessed 26 June 2020).
- [63] Allresist. *Positive e-beam resists AR-P 6200 (CSAR 62)*. Available at [https://www.allresist.com/wp-content/uploads/sites/2/2020/02/allresist\\_produkinfos\\_ar-p6200\\_english.pdf](https://www.allresist.com/wp-content/uploads/sites/2/2020/02/allresist_produkinfos_ar-p6200_english.pdf) (Accessed 26 June 2020).
- [64] Allresist. *Protective coating PMMA Electra 92 (AR-PC 5090)*. Available at [https://www.allresist.com/wp-content/uploads/sites/2/2016/12/allresist\\_produkinfos\\_ar-pc5090-5091\\_english.pdf](https://www.allresist.com/wp-content/uploads/sites/2/2016/12/allresist_produkinfos_ar-pc5090-5091_english.pdf) (Accessed 26 June 2020).

- [65] Chang, T. H. P. Proximity effect in electron-beam lithography. *Journal of Vacuum Science and Technology*, 12 (6), **1975**, pp. 1271–1275. doi:[10.1116/1.568515](https://doi.org/10.1116/1.568515).
- [66] Ha, S., Janissen, R., Ussembayev, Y. Y., *et al.* Tunable top-down fabrication and functional surface coating of single-crystal titanium dioxide nanostructures and nanoparticles. *Nanoscale*, 8, **2016**, pp. 10739–10748. doi:[10.1039/C6NR00898D](https://doi.org/10.1039/C6NR00898D).